Journal of Medicinal Chemistry

pubs.acs.org/jmc

Drug Annotation

Discovery of AG-270, a First-in-Class Oral MAT2A Inhibitor for the Treatment of Tumors with Homozygous *MTAP* Deletion

Zenon Konteatis,*,# Jeremy Travins,# Stefan Gross, Katya Marjon, Amelia Barnett, Everton Mandley, Brandon Nicolay, Raj Nagaraja, Yue Chen, Yabo Sun, Zhixiao Liu, Jie Yu, Zhixiong Ye, Fan Jiang, Wentao Wei, Cheng Fang, Yi Gao, Peter Kalev, Marc L. Hyer, Byron DeLaBarre, Lei Jin, Anil K. Padyana, Lenny Dang, Joshua Murtie, Scott A. Biller, Zhihua Sui, and Kevin M. Marks

Cite This: *J. Med. Chem.* 2021, 64, 4430−4449

Read Online

ACCESS | Metrics & More | Article Recommendations | Supporting Information

ABSTRACT: The metabolic enzyme methionine adenosyltransferase 2A (MAT2A) was recently implicated as a synthetic lethal target in cancers with deletion of the methylthioadenosine phosphorylase (*MTAP*) gene, which is adjacent to the *CDKN2A* tumor suppressor and codeleted with *CDKN2A* in approximately 15% of all cancers. Previous attempts to target MAT2A with small-molecule inhibitors identified cellular adaptations that blunted their efficacy. Here, we report the discovery of highly potent, selective, orally bioavailable MAT2A inhibitors that overcome these challenges. Fragment screening followed by iterative structure-guided design enabled >10 000-fold improvement in potency of a family of allosteric MAT2A inhibitors that are substrate noncompetitive and inhibit release of the product, *S*-adenosyl methionine (SAM), from the enzyme's active site. We demonstrate that potent MAT2A inhibitors substantially reduce SAM levels in cancer cells and selectively block proliferation of *MTAP*-null cells both in tissue culture and xenograft tumors. These data supported progressing **AG-270** into current clinical studies (ClinicalTrials.gov NCT03435250).

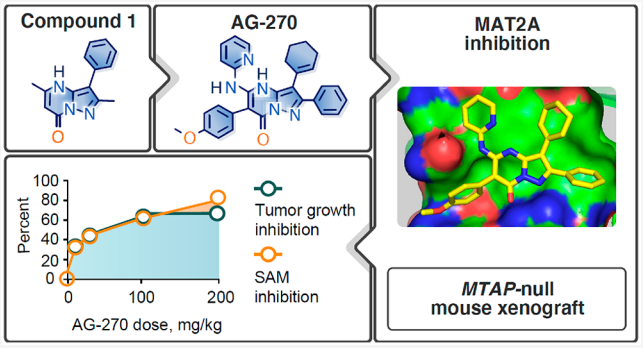

INTRODUCTION

The methylthioadenosine phosphorylase (*MTAP*) gene is located adjacent to the *CDKN2A* tumor suppressor and is codeleted with *CDKN2A* in approximately 15% of all cancers, leading to aggressive tumors with poor prognoses for which no effective molecularly targeted therapies exist.[1−4] The metabolic enzyme methionine adenosyltransferase 2A (MAT2A) has an important role in metabolism and epigenetics because it is the primary producer of the universal methyl donor *S*-adenosyl methionine (SAM). Recent work has demonstrated that depletion of MAT2A using RNA interference leads to a selective antiproliferative effect in cancers with deletion of *MTAP*.[2,5,6] A simple explanation for this selective vulnerability has been described, in which the activity of the SAM-utilizing type II protein arginine *N*-methyltransferase 5 (PRMT5) is inhibited by the *MTAP* substrate, 5′-methylthioadenosine (MTA), which accumulates when *MTAP* is deleted. Within this tumor environment, the catalytic activity of the PRMT5 enzyme is reduced, and it becomes vulnerable to further inhibition by reduction of SAM levels, whereas its activity in normal tissues and *MTAP*-proficient tumors remains largely unaffected.[2]

Although these results suggest that targeting MAT2A may prove beneficial in *MTAP*-deleted cancers, past efforts to devise effective MAT2A inhibitors have been challenging. Methionine analogues such as cycloleucine[7,8] as well as stilbene derivatives[9] have been reported in the literature to be inhibitors of MAT2A; however, their weak biochemical potency (>10 μM) and very weak cellular activity did not enable their development into useful therapeutics. The recent discovery of a moderately potent allosteric MAT2A inhibitor, PF-9366,[10] demonstrates the potential to drug MAT2A via an allosteric mechanism. Unfortunately, PF-9366 treatment in cells induced cellular adaptation, particularly upregulation of MAT2A itself, which blunted cellular potency and led to inadequate antiproliferative effects.

Herein, we describe the drug discovery efforts that led to the identification of **AG-270**, a first-in-class, orally bioavailable MAT2A inhibitor currently in clinical development (ClinicalTrials.gov NCT03435250). This class of MAT2A

Received: November 2, 2020
Published: April 8, 2021

Downloaded via 136.158.32.33 on May 14, 2021 at 02:26:04 (UTC).
See https://pubs.acs.org/sharingguidelines for options on how to legitimately share published articles.

ACS Publications

© 2021 American Chemical Society

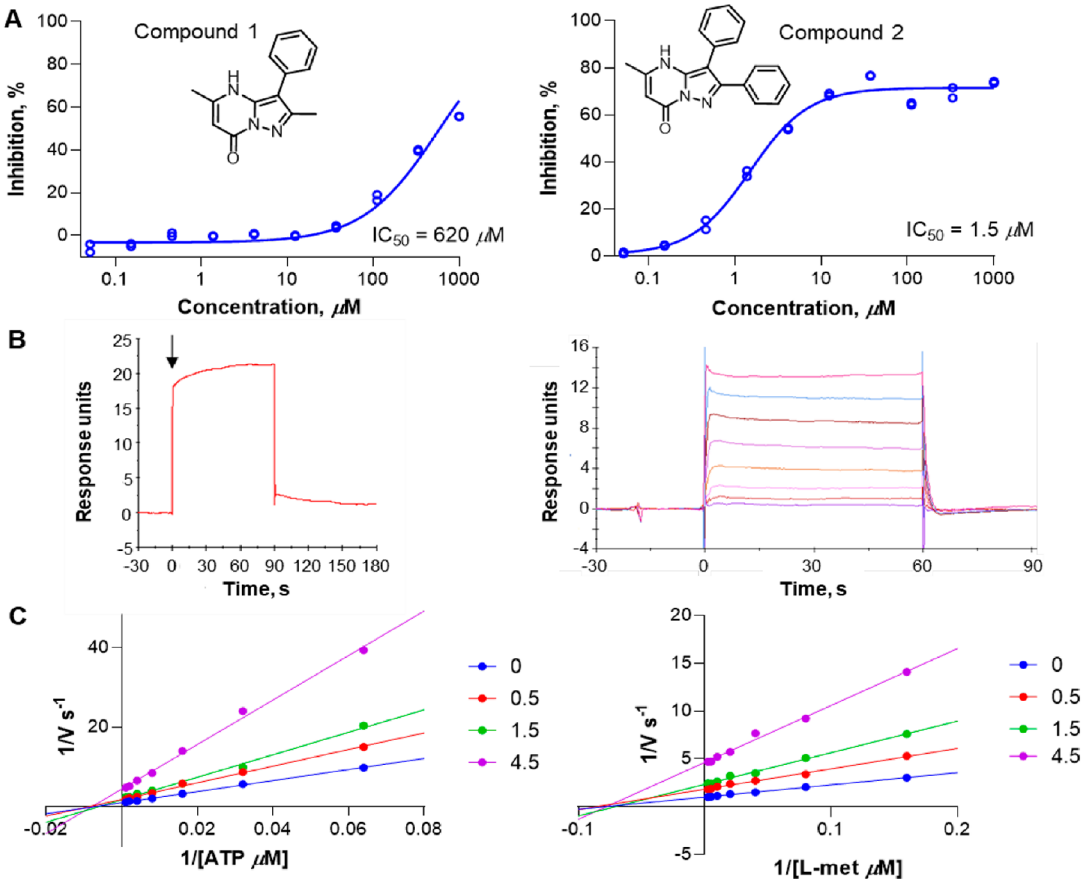

Figure 1. Hit identification. (A) MAT2A enzyme inhibition IC_{50} (μM). Values are the mean of three experiments. (B) Surface plasmon resonance sensorgrams (the result of only one experiment each shown). (C) Mechanism of action study demonstrates compound **2** is noncompetitive with regard to ATP and L-methionine substrates; test concentrations of **2** were 0.5, 1.5, and 4.5 μM.

inhibitors is allosteric, substrate noncompetitive, and inhibits MAT2A activity by preventing product release. We also report findings from preclinical studies describing the *in vitro* and *in vivo* characterization of this class of inhibitors with a focus on our clinical molecule **AG-270**.

RESULTS AND DISCUSSION

Identification of MAT2A Inhibitors via Fragment Screening. We screened a library of >2000 fragments for the ability to bind to the MAT2A protein dimer using a mass spectrometry-based ultrafiltration assay.[11] Thirty-one fragment hits were identified, a modest 1.55% hit rate, which were then validated in orthogonal enzymatic and surface plasmon resonance (SPR) assays. Of these fragments, compound **1** showed weak enzymatic inhibition of MAT2A at 620 μM (Figure 1A), which was consistent with a weak SPR sensorgram (Figure 1B). A hit expansion similarity search (Tanimoto >80%; 350 < MW > 200) was carried out, and 54 commercially available compounds were purchased and tested for enzymatic inhibition of MAT2A, followed by SPR binding. Among the virtual hits, **2** was identified as the most potent MAT2A inhibitor (Figure 1A), having an IC_{50} of 1.5 μM and showing a robust, dose dependent SPR signal with a dissociation constant (K_D) of 70 μM (Figure 1B). Detailed kinetic analysis[12] with compound **2** demonstrated a non-competitive inhibition modality with regard to both ATP and L-methionine, suggesting a binding location outside the catalytic active site (Figure 1C).

We cocrystallized compound **2** with the MAT2A protein in complex with SAM (MAT2A·SAM·**2**) and determined the structure of this ternary complex at atomic resolution of 1.14 Å (Supporting Information Table S1). We observed two copies of **2** bound at the interface of the obligate MAT2A dimer, one molecule of **2** per monomer of MAT2A, in the same allosteric pocket as previously reported for PF-9366[10] (Figure 2).

Compound **2** forms key interactions with MAT2A, including bidentate hydrogen bonds from the amide carbonyl and the nitrogen of the pyrazole of **2** to the guanidino group of Arg335, and two hydrophobic van der Waals contacts between the two phenyl groups of **2** and the protein. Another observation in this crystal structure is the desolvation of the allosteric pocket upon binding of the inhibitor. Whereas the unliganded pocket contains multiple water molecules extending out to the solvent front (PDB code: 2P02),[13] this liganded structure contains only a few remaining water molecules. Importantly, this cocrystal structure determined in the presence of SAM molecules bound in the MAT2A active sites demonstrates that the inhibitor binding traps the reaction product by closure of the α helix gates (Figure 3A). This confirms the mode of action to be enhanced inhibition of enzyme product (SAM) release, consistent with our kinetic studies demonstrating a noncompetitive mechanism-of-action. These interactions are reflected in the increase in enzymatic potency and established this pyrazolo[1,5-*a*]pyrimidin-7(4*H*)-one class as worthwhile for further exploration. The five substituents pursued in this SAR campaign are shown in Figure 2C.

https://doi.org/10.1021/acs.jmedchem.0c01895
J. Med. Chem. 2021, 64, 4430−4449

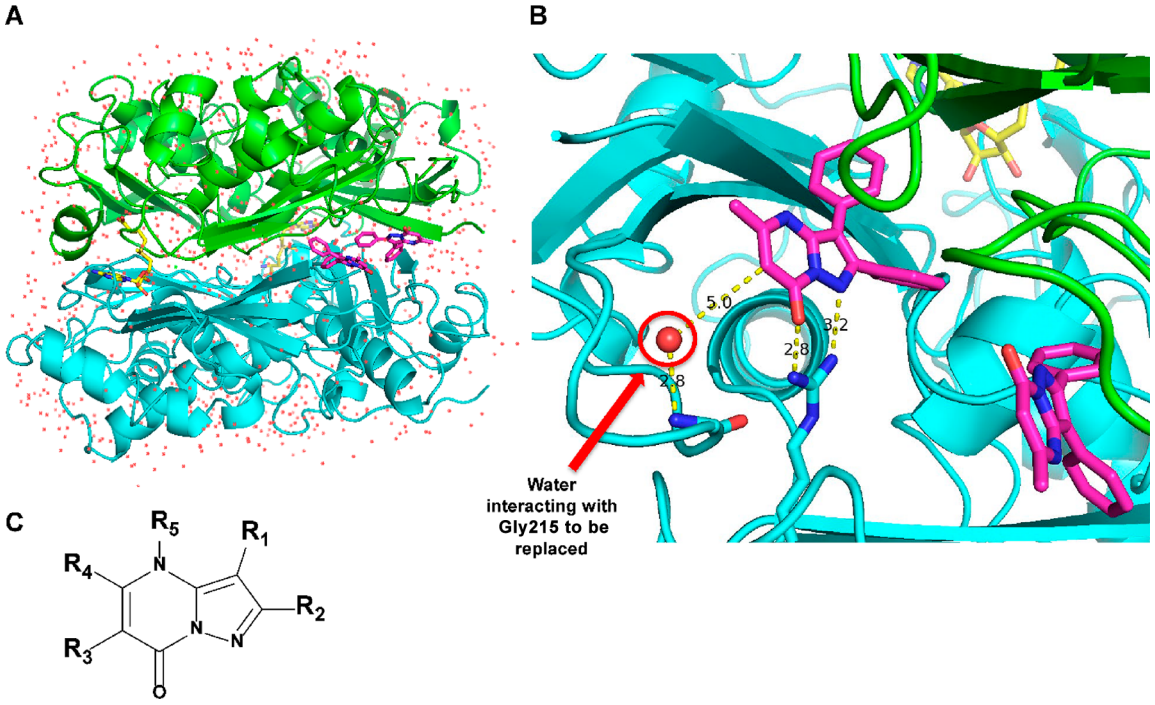

Figure 2. Cocrystal structure of compound **2** with MAT2A and reaction product SAM (PDB code 7KCE). (A) Homodimeric form of MAT2A with two protein chains shown in green and cyan, respectively. SAM molecules, in yellow, are in the active site and compound **2**, in magenta, is in an allosteric site. (B) Allosteric binding site of MAT2A. Compound **2**, in magenta, and water interacting with residue Gly215 in red sphere. (C) Structural class pyrazolo[1,5-*a*]pyrimidin-7(4H)-one and all the substituents to be explored in the SAR campaign.

Structure-Based Design Leading to Potent, *MTAP*-Null Selective MAT2A Inhibitor AGI-24512. The cocrystal structure of **2** indicated that mostly hydrophobic residues occupied regions of the binding site surrounding R_1 and R_2 substituents of **2**. This led to targeted substituents at the R_1 and R_2 positions to establish initial SARs for this series. Attempts to increase polarity in substituent R_1 by modifying the phenyl group to 2-pyridine in **3** or to 2-furan in **4** led to modest losses in potency (Table 1). Alternatively, increasing hydrophobicity and sp^3 (aliphatic carbons) character led to improvements in enzymatic potency, as shown in **5**−**8**. We rationalized that piperidine could be a good structural homologue of cyclohexene (**7**), and indeed, **9** maintained good potency at 0.26 μM.

Initial exploration of the R_2 group centered around probing the properties of the R_2 binding pocket. Replacing phenyl with heterocycles in **10** (2-furan), **11** (4-pyrazole), and **13** (2-thiazole) led to significant decreases in potency, suggesting that polarity in R_2 substituents was not tolerated in this nonpolar pocket. Nonaromatic moieties such as cyclohexene (**12**) led to large losses in enzymatic potency (Table 2). Only **14** (3-hydroxyphenyl) and **15** (3-fluorophenyl) maintained similar potency to **2**, indicating a preference for aromatic groups in this highly hydrophobic subpocket.

A cell assay using HCT116 *MTAP*-null cells was developed to assess MAT2A inhibition in cancer cells by measuring the abundance of the MAT2A product SAM following treatment with increasing concentrations of the more potent compounds. Compounds **14**, **5**, and **7** showed increasing cellular potency (Supporting Information Figure S1, Tables 1 and 2) in line with their biochemical potency, suggesting that the two assays were correlated and thus validating the cellular assay.

The MAT2A-**2** cocrystal structure (Figure 2B) showed a water molecule interacting with the N−H of the protein residue Gly215, and this water-436 was within 5 Å of the core of the pyrazolo-pyrimidinone scaffold. Using structure-based design,[14] we added a phenol substituent attached at the C-6 position of the scaffold to replace this water interaction. We made this R_3 modification using **9** as the core because it had better solubility than **2** (Table 1). The resulting analogue, **AGI-24512**, showed improved potency with an enzymatic IC_{50} of 8 nM. Mode of action enzymatic studies were carried out, confirming that AGI-24512, like compound **2**, is non-competitive with respect to both ATP and L-Met (Supporting Information Figure S2). A few close analogues of **AGI-24512** were synthesized to establish the value of this new interaction (Table 3). The addition of a phenyl ring at R_3 (**16**) showed 0.15 μM enzymatic inhibition, while the 4-pyridyl (compound **17**) had an IC_{50} of 0.160 μM and a thiazole analogue (**18**) was much less active. Only the 3-pyrazolyl substitution (**19**) maintained acceptable potency, presumably by still interacting with Gly193 via a water bridge (Table 3).

The structure of the ternary complex of MAT2A bound to SAM and **AGI-24512** (MAT2A·SAM·**AGI-24512**) was determined at 1.10 Å resolution (Supporting Information Table S1) and confirmed both the allosteric binding site and the predicted replacement of the interaction with water-436 by the phenol substituent at R_3 (Figure 3B). Additional interactions are made by the piperidine group at the C-3 position of the scaffold, which is encased in a hydrophobic protein environment created by residues Phe18, Phe20 of one protomer, and Phe139, Ser331, Phe333, and Leu315 of the adjacent chain MAT2A dimer (Figure 3B and C). The atomic resolution cocrystal structure also permitted assessment of the effects of inhibitor binding on the active site of MAT2A. The active site possesses a loop−α-helix−loop arrangement that caps the entrance to the active site and closes upon SAM binding (Figure 3A and D [SAM-free structure, PDB code

https://doi.org/10.1021/acs.jmedchem.0c01895
J. Med. Chem. 2021, 64, 4430−4449

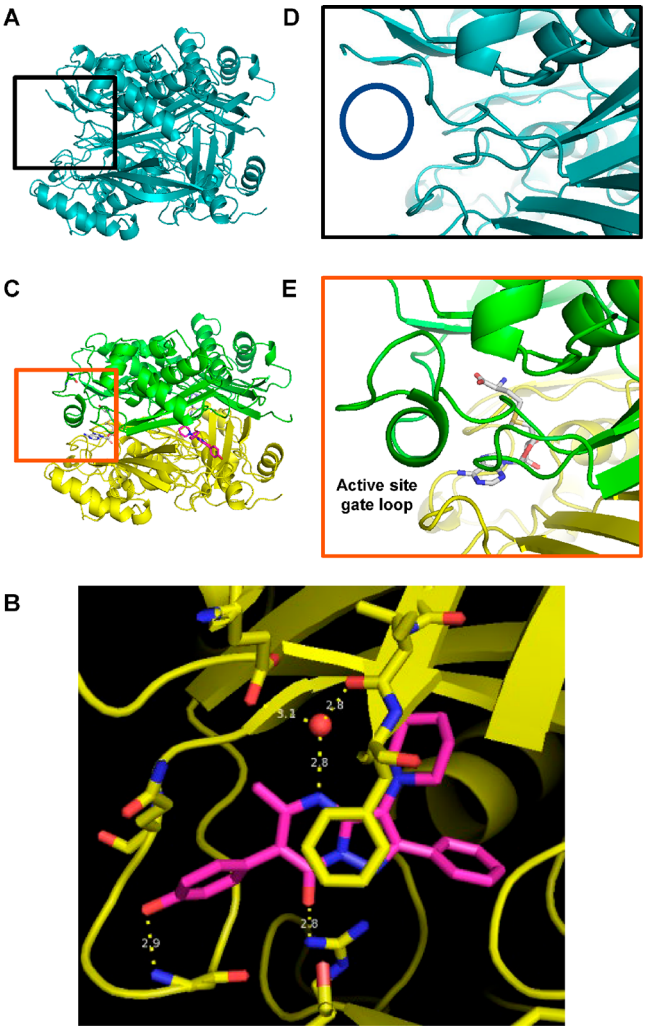

Figure 3. Cocrystal structure of MAT2A·SAM·**AGI-24512**. (A) Crystal structure of MAT2A SAM free form (PDB code: 5A19). (B) Close-up of the allosteric binding site, highlighting **AGI-24512** and its interactions with MAT2A protein and a key water molecule. (C) The current crystal structure obtained with **AGI-24512** in the presence of SAM (PDB code 7KCF). (D) Close-up of the apo-MAT2A region indicating the "open" form of the α-helix gate that is unstructured in the absence of SAM. (E) Close-up of the active site gate loop (protein in green and yellow, SAM in atom color).

5A19][15] vs Figure 3C and E [inhibitor-bound structure]). In all the inhibitor-bound MAT2A cocrystal structures, we observed SAM in the active site and the gate loop preserved in the closed position (Figure 3E).

This lead compound, **AGI-24512**, was fully characterized in cellular assays and became an important *in vitro* tool that enabled further cellular studies to evaluate MAT2A biology.[16] **AGI-24512** treatment in the HCT116 *MTAP*-null cell assay led to a dose-dependent decrease in SAM levels with an IC_{50} of 100 nM (Table 3). **AGI-24512** also demonstrated *MTAP*-null selective antiproliferative activity in an HCT116 engineered cell model.[16] Consistent with prior results with PF-9366,[10] we observed upregulation of MAT2A protein upon treatment with **AGI-24512**. Notably, this pathway feedback mechanism did not prevent the antiproliferative activity of **AGI-24512**. We hypothesized that the improved potency of **AGI-24512** relative to prior MAT2A inhibitors, i.e. PF-9366, enabled **AGI-24512** to maintain antiproliferative effects despite this cellular adaptation. This pharmacological selective reduction of growth of *MTAP*-null genotype cancer cells confirms our previous observations using genetic tools targeting MAT2A,[2] suggesting that pharmacologic inhibition of MAT2A enzymatic function represents a viable therapeutic approach with potential for a superior therapeutic window by sparing the *MTAP*-WT noncancerous tissue. A variety of further biological studies with **AGI-24512** are discussed in a recent publication.[16]

Discovery of *in Vivo* Lead Candidate AGI-25696. Initial assessment of the pharmacokinetic properties of **AGI-24512** indicated poor oral absorption and a short half-life in rats. At the same time, both mouse and human *in vitro* metabolite identification studies of **19** indicated, as expected, that the piperidine ring at R_1 was mostly responsible for the poor liver microsomal stability exhibited (human microsomal extraction ratio, ER, 0.72, Supporting Information Figure S3). The focus in these experiments was to identify major metabolites to aid appropriate design to reduce metabolism or abrogate any specific metabolic pathways. All compounds at this stage showed rapid oxidative metabolism across preclinical species and human microsomes, so we set out to improve metabolic stability. We first sought to generate analogues in the R_3 position that contain other hydrogen-bond acceptors to investigate their ability to maintain enzymatic potency while improving their metabolic stability. Compounds **20**–**23** maintained reasonable enzymatic potency but did not improve microsomal stability (ER, Table 4). We revisited **24**, an earlier analogue of **AGI-24512**, which had a phenyl group in place of the piperidine at R_1 and showed better metabolic stability with a human microsomal ER of 0.54. The next set of analogues kept the quinoline at R_3 and modified R_1 with all the previously identified potency-enhancing substituents (**25**–**27** and **AGI-25696**). While most compounds showed good enzymatic potency, only **AGI-25696**, which incorporated the phenyl substituent at R_1, gave a very stable analogue with human microsomal ER of 0.16 (Table 4). This first metabolically stable analogue showed good cellular activity at 150 nM (Figure 4A, HCT116 cell assay, SAM IC_{50}) and was further profiled *in vivo*.

Oral treatment of tumor-bearing mice with **AGI-25696** led to sustained high exposure in pancreatic KP4 *MTAP*-null xenograft tumors (Figure 4B; maximum serum concentration [C_{max}] of 179 000 ± 21 500 ng/mL and 32 300 ± 6100 ng/g; AUC_{0-12h} of 1 650 000 and 372 000 h.ng/g in plasma and tumor, respectively, after 3 b.i.d. doses). To test whether *MTAP*-null tumors are sensitive to the antiproliferative effects of MAT2A inhibition *in vivo*, **AGI-25696** was given orally once daily (q.d.) to mice bearing subcutaneous KP4 *MTAP*-null xenografts. A high dose of 300 mg/kg was given to ensure a result would be obtained for proof of principle demonstration. Consistent with *in vitro* data, compound treatment led to a substantial reduction in growth of KP4 *MTAP*-null xenografts (tumor growth inhibition [TGI] = 67.8%, p = 0.0001, Figure 4C) with no adverse effects on mouse body weight throughout the 33 day study (Figure 4D). Having established *in vivo* proof of principle in this mouse study, the emphasis shifted to improving physical properties (Figure 4A) and cellular activity to produce a compound with the potential for clinical development.

Discovery of Clinical Candidate AG-270. AGI-25696 had very high PPB (>99.9% in human plasma measured by ultracentrifugation, Figure 4A) and a high efflux ratio in a Caco-2 assay (6.0, Figure 4A), which projected to a very high

https://doi.org/10.1021/acs.jmedchem.0c01895
J. Med. Chem. 2021, 64, 4430−4449

Table 1. R_1 Modifications[a]

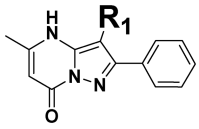

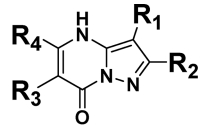

Compound	Structure of R_1	Enzymatic MAT2A IC_{50} (μM)	Enzymatic MAT2A maximal inhibition (%)	Solubility pH2/pH7.4 (μM)	4 h cell *MTAP*-null SAM IC_{50} (μM)	Cell maximal inhibition (%)
2	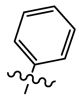	1.50	69	-	-	-
3	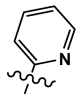	7.1	79	-	-	-
4		3.66	90	-	-	-
5		1.14	84	-	0.588	82
6		0.68	88	-	-	-
7		0.26	85	<0.5/<0.5	0.106	72
8	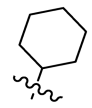	0.66	59	-	-	-
9	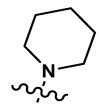	0.26	86	61/3	-	-

[a]Values are the mean of three experiments.

dose for adequate human exposure. The weakly acidic nature of this chemotype, driven by the tautomerism described in Figure 5, was hypothesized to contribute to the high plasma protein binding. The pyrazolo[1,5-*a*]pyrimidin-7(4H)-one (A) scaffold can easily tautomerize to both the pyrazolo[1,5-*a*]pyrimidin-7-ol (B) and the pyrazolo[1,5-*a*]pyrimidin-7(1H)-one (C), giving rise to various potential modes of binding to plasma proteins because the acidic proton can locate at three different positions.

***N*-Methylation of the Core Reduces Human PPB but Decreases Percentage Maximal Inhibition.** Indeed, the *N*-methylated analogues **28** and **29** (Table 5, $R_5 = CH_3$), where the acidic proton was eliminated and tautomerization was prevented, showed reduced PPB relative to their corresponding R_5 = H counterparts (compare free fraction of 0.09% for **AG-24512** with 1.54% for **28** and 0.03% for **AGI-25696** with 0.9% for **29**, as shown in Table 5). However, analogues **28** and **29** showed dramatic decreases in the percent maximal inhibition[12] of MAT2A from >90% to <70%. This trend was observed with other R_5 analogues (not reported here), and thus, this strategy for improving free fraction was not successful in maintaining full efficacy of the inhibitors. Throughout this discovery program, the enzymatic allosteric inhibition IC_{50} correlated very well with the 72 h cell assay EC_{50} but not with the percent maximal inhibition, as expected for the mechanism (Supporting Information Figure S4).

Masking of Core N−H by Intramolecular Hydrogen Bond Improves Percentage Maximal Inhibition but Affects Other ADME Parameters. During the early SAR development phase of the program, R_4 substituent variations

https://doi.org/10.1021/acs.jmedchem.0c01895
J. Med. Chem. 2021, 64, 4430−4449

Table 2. R_2 Modifications[a]

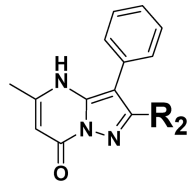

Compound	Structure of R_2	Enzymatic MAT2A IC_{50} (μM)	Enzymatic MAT2A maximal inhibition (%)	4 h cell *MTAP*-null SAM IC_{50} (μM)	Cell maximal inhibition (%)
2	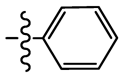	1.50	69	-	-
10	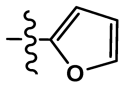	50.1	65	-	-
11	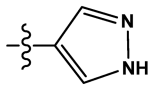	No fit	No fit	-	-
12	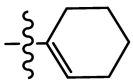	78.8	55	-	-
13	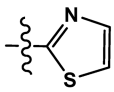	12.2	63	-	-
14	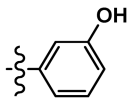	1.90	92	7.65	75
15	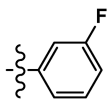	1.34	76	-	-

[a]Values are the mean of three experiments. No fit = no activity.

were explored with R_1 and R_2 = Ph and R_3 = H. Among the analogues explored (represented by **30**−**34**, Table 6; additional analogues not shown), only **34** exhibited better potency than **2** and increased percent maximal inhibition from partial to 88%. Encouraged by this result, we determined the cocrystal structure of this analogue with MAT2A (MAT2A·SAM·**34**) at 1.24 Å resolution (Supporting Information Table S1). New interactions were noted between the amide carbonyl of residue Gln190 and the N−H at R_4, the backbone carbonyl of Ile332 with the hydrogen of the pyrazole of R_4, along with an intramolecular hydrogen bond between the sp^2 (aromatic) nitrogen of the R_4 pyrazole and the N−H at R_5 shown in Figure 6A. This intramolecular hydrogen bond was then hypothesized to be responsible for the improved maximal inhibition (Table 6) and lowering human PPB (Table 6) by masking the acidic hydrogen on the scaffold. This strategy then became a more viable approach toward inhibitors with maximal inhibition and lower human PPB than *N*-methylation. Similar internal hydrogen-bonding strategies have been employed in medicinal chemistry to mask polarity and have been exploited to improve some physicochemical parameters of multiple structural classes.[17−19]

Analogue **35**, bearing a 4-hydroxyphenyl group at R_3, showed low nanomolar enzymatic potency and high percent

https://doi.org/10.1021/acs.jmedchem.0c01895
J. Med. Chem. 2021, 64, 4430−4449

Table 3. R_3 Exploration[a]

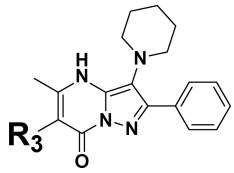

Compound	Structure of R_3	Enzymatic MAT2A IC_{50} (μM)	Enzymatic MAT2A maximal inhibition (%)	72 h cell *MTAP*-null SAM IC_{50} (μM)
9		0.26	86	-
16	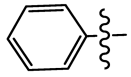	0.150	93	-
17	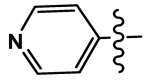	0.158	91	-
18	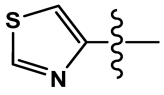	1.31	85	-
19	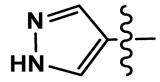	0.057	95	-
AGI-24512	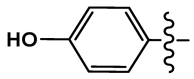	0.008	91	0.100

[a]Values are the mean of three experiments.

maximal inhibition (Table 7). The cocrystal structure of this compound (MAT2A·SAM·**35**) was determined at 1.24 Å resolution, confirming the expected binding mode (Figure 6B). Gratifyingly, all of the interactions observed in the crystal structures of **34** and **AGI-24512** were maintained in **35**, validating the cumulative structural understanding of MAT2A−inhibitor interactions. Analogues of **35** were synthesized, varying both R_1 and R_3 while keeping the amino pyrazole substituent at R_4 (Table 7). Characterization of these advanced compounds included cellular assays that measured SAM production in *MTAP*-null cells at 72 h to account for the MAT2A upregulation as well as cellular proliferation assays. Microsomal stability and PPB were also measured. All compounds in this subseries had excellent enzymatic potency (4−14 nM) and maximal inhibition (92−96%) but either poor inhibition of cell proliferation (**35**, **36**, **39**) or moderate mouse and human microsomal stability (**37** and **38**). Another deficiency of these analogues was the very high PPB observed for all members of this subseries (>99.5%, Table 7).

Masking Core N−H and Decreasing the Number of Hydrogen-Bond Donors Leads to AG-270. The successful masking of polarity by internal hydrogen bonding encouraged further modifications at R_4. However, the presence of the additional hydrogen-bond donor in this region presented a new challenge for permeability, both masking polarity and decreasing the number of hydrogen-bond donors needed to be pursued concomitantly. The N−H in the pyrazole ring of **36** was protected via an ethyl carbamate to give **40**, which maintained enzymatic and cellular potency and showed mildly improved activity in the cell proliferation assay (Table 8). Oxadiazole ester **41** also showed good enzymatic potency and percent maximal inhibition, establishing that the second hydrogen bond to the backbone carbonyl of residue Ile332 was not contributing much to the potency of the earlier inhibitors. This finding led to a subseries of analogues containing over 70 heterocycles in the R_4 position. Some of these are reported in Table 8 as representatives of the results obtained. The 3-amino-isoxazole substitution (**42**) maintained good potency and occupancy in the enzymatic assay but

https://doi.org/10.1021/acs.jmedchem.0c01895
J. Med. Chem. 2021, 64, 4430−4449

Table 4. Further R_3 Exploration

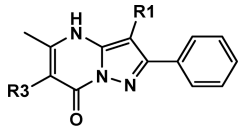

Compound	Structure of R_3	Structure of R_1	Enzymatic MAT2A IC_{50} (μM)	Enzymatic MAT2A maximal inhibition (%)	ER, HLM
AGI-24512	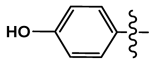		0.008	91	0.66
20	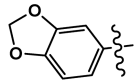		0.081	93	0.83
21	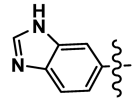		0.045	92	0.79
22	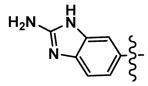		0.083	94	0.75
23	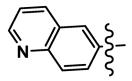		0.052	95	0.88
24	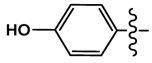		0.033	93	0.54
25	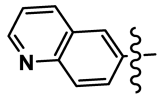		0.066	93	0.66
26	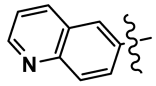		0.025	96	0.70
27	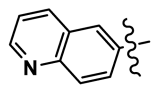		0.159	96	0.64
AGI-25696	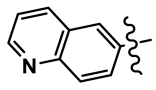	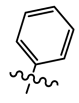	0.097	95	0.16

[a]Values are the mean of three experiments. ER = extraction ratio; HLM = human liver microsome.

showed weaker cell activity and poor inhibition of HCT116 *MTAP*-null cell proliferation. However, microsomal stability was excellent, and PPB was much improved to the level previously seen for the *N*-methyl analogues at R_5 (98.92%, Table 8). Similar trends were observed with a variety of analogues, exemplified here by the 2-pyridine (**43**) and the 2-pyridazine (**44**), demonstrating good enzymatic and cellular potency, excellent microsomal stability, and good free fraction,

https://doi.org/10.1021/acs.jmedchem.0c01895
J. Med. Chem. 2021, 64, 4430−4449

A

Parameter	AGI-25696
Enzyme IC_{50} MAT2A (nM)	97
HCT116 cell SAM IC_{50} 72 h (nM)	150 (84% inh)
ER, HLM / MLM	0.16 / stable
Caco2, A>B/Efflux (10^{-6} cm/s)	6.75 / 6.0
PPB, human / mouse (%)	>99.9 / 99.9
Solubility, pH2 / pH7.4 (μM)	67 / 15

B

Parameter	Plasma	Tumor
C_{max} (ng/mL)	179,000 ± 21,500	32,300 ± 6100
$AUC_{0\text{-}12h}$ (h.ng/g)	1,650,000	372,000

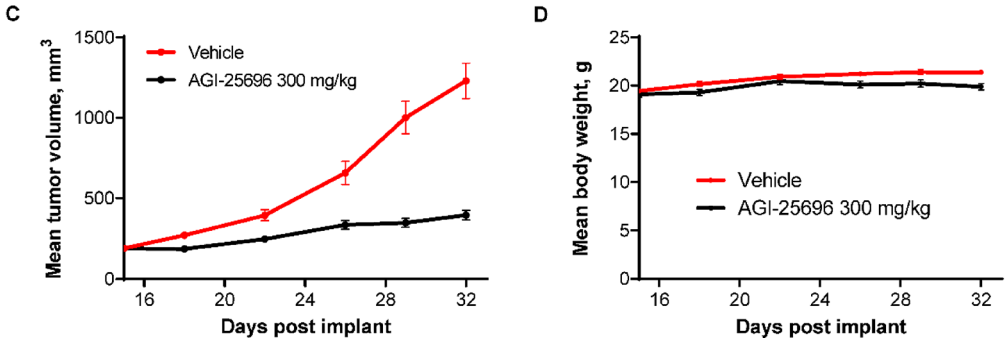

Figure 4. Pharmacologic targeting of MAT2A with *in vivo* tool molecule selectively blocks growth of *MTAP*-null tumors *in vivo*. Fifteen mice per arm (total 30 animals) were used in this study. (A) Key *in vitro* parameters of **AGI-25696**. (B) PK data from the study after 3 b.i.d. doses. (C) Mean tumor volume in mice inoculated with KP4 *MTAP*-null pancreatic cells treated daily with 300 mg/kg **AGI-25696** (black line) or vehicle (red line). (D) Mean body weight of the mice. Error bars show standard error of the mean. HLM, human liver microsomes; MLM, mouse liver microsomes.

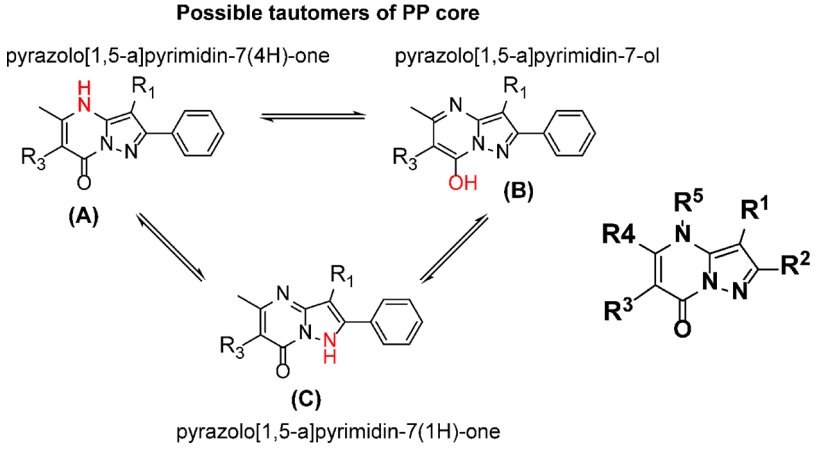

Figure 5. Are tautomers responsible for the physical chemistry properties? Hypothesis: three possible tautomers of the pyrrolopyrimidinone scaffold (A–C) share the acidic proton in different locations of the scaffold, which can potentially increase the ability of each compound to bind to plasma proteins.

but weak inhibition of HCT116 *MTAP*-null cell proliferation (Table 8). Pyridine at R_4 showed a higher free fraction than pyridazine at R_4, presumably due to the better intramolecular hydrogen bond with the hydrogen in the core structure. The compound with the best overall combination of potency and drug-like properties was **AG-270**, combining the 2-pyridine at R_4 with the cyclohexene at R_1. The measured pK_a of AG-270 was 8.56, a substantial increase from the measured pK_a of 6.3 for AGI-25696. The impact of masking the acidic hydrogen (pK_a = 6.3) by the intramolecular interaction from the 2-pyridine of the R_4 substituent was to stabilize the tautomers to mostly the desired one, where the hydrogen remained on the core nitrogen at R_5. This resulted in good potency in both enzymatic and cellular assays while increasing the free fraction to 1.54% (Table 8).

The cocrystal structure of MAT2A·SAM·**AG-270** was determined at 1.32 Å resolution (Supporting Information Table S1) and confirmed the designed mode (Figure 7).

The expected interactions as seen in the cocrystal structure of **35** were maintained and the internal hydrogen bond was validated, suggesting that the bound conformation is a low energy conformer of AG-270. Energy calculations on this bioactive conformation confirmed that it is either at the global minimum or near it, based on the method used (LowModeMD or systematic, Supporting Figure S5).[14] The only ligand–protein interaction changes were the absence of the hydrogen

https://doi.org/10.1021/acs.jmedchem.0c01895
J. Med. Chem. 2021, 64, 4430–4449

Table 5. *N*-Methylation Improves Human PPB Free Fraction[a]

Compound	Structure	Enzymatic MAT2A IC_{50} (μM)	Enzymatic MAT2A maximal inhibition (%)	Human PPB, (% bound, % free)
AGI-24512	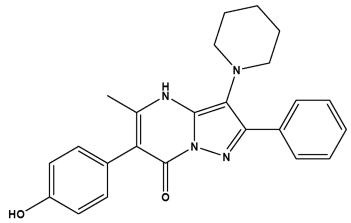	0.008	91	99.9, 0.09
28	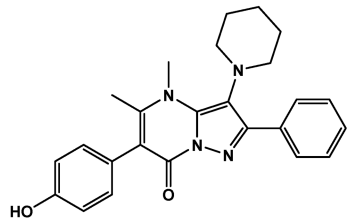	0.102	66	98.46, 1.54
AGI-25696	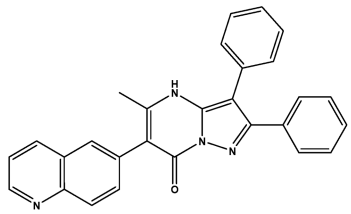	0.097	95	99.97, 0.03
29	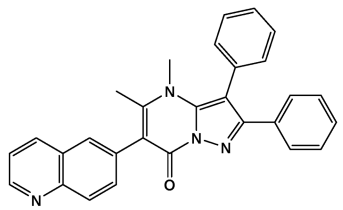	0.120	61	99.1, 0.9

[a]By removing the acidic proton via *N*-methylation, tautomerism is no longer possible, as seen in Figure 5, and the free fraction of compounds **28** and **29** increases.

bond from the compound to Ile332 and a new hydrophobic interaction between the 2-pyridine group at R_4 and the MAT2A protein residues. These modifications led to the good potency in *in vitro* assays. **AG-270** demonstrated potent reduction in levels of intracellular SAM, as well as *MTAP*-null–selective antiproliferative activity in the HCT116 *MTAP* isogenic cell model *in vitro* (Table 8).[16] Further biochemical studies confirmed that **AG-270** maintained the same mode of action as Compound **2** and **AGI-24512**, being noncompetitive with respect to both ATP and L-Met (Supporting Information Figure S2).

AG-270 was further characterized for ADME properties, *in vitro* ancillary pharmacology, and oral bioavailability. The properties of **AG-270** (Table 9) were favorable overall, including high microsomal stability and an improved plasma free fraction (Table 8). However, **AG-270** showed low solubility and indeterminable permeability in the Caco-2 assay due to low recovery. Low solubility was addressed by using spray dried dispersion,[20] which resulted in good oral bioavailability across species (monkey 31%, dog 48%, rat 92%; Table 9 and Supporting Information Figure S6, Table S2). Compounds synthesized in this program had variable solubility that was not related to the calculated distribution coefficient

https://doi.org/10.1021/acs.jmedchem.0c01895
J. Med. Chem. 2021, 64, 4430−4449

Table 6. R_4 Exploration[a]

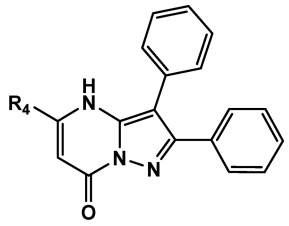

Compound	Structure of R_4	Enzymatic MAT2A IC_{50} (μM)	Enzymatic MAT2A maximal inhibition (%)
2		1.5	69
30		3.66	54
31	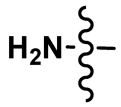	No fit	-
32	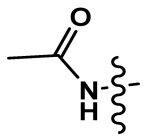	4.11	85
33	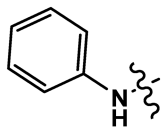	16.6	70
34	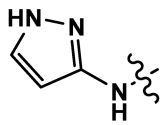	0.27	88

[a]Values are the mean of three experiments.

(between octanol and water) of ionizable compounds (Supporting Information Figure S7), or any other easily understood parameter, so empirical data guided the efforts. **AG-270** showed excellent microsomal, hepatocyte, and *in vivo* metabolic stability across species (human, mouse, rat, dog, and monkey; Table 9). No overly concerning off-target activities in the standard battery of *in vitro* ancillary pharmacology assays (Eurofins Discovery 95 biochemical screen assays, hERG, CYP450, PXR, Ames test) were observed for this compound. The only liabilities of **AG-270** identified were inhibition of UGT1A1 (IC_{50} of 1.1 μM) which could lead to elevation of bilirubin, and of the hepatocyte transporter OATP1B1 (IC_{50} of 2.1 μM). The overall superior properties of **AG-270** led to its selection for detailed *in vivo* profiling.

Oral administration of **AG-270** at 200 mg/kg q.d. in a pancreatic KP4 *MTAP*-null xenograft mouse model for 38 days led to sustained high-level exposure in plasma (Figure 8A, solid line, data from last 24 h of the study) with corresponding reductions in levels of tumor SAM (Figure 8A, dashed line). In this multiday study, **AG-270** was administered at multiple dose levels to test whether *MTAP*-deleted tumors are sensitive to the antiproliferative effects of MAT2A inhibition *in vivo*.

https://doi.org/10.1021/acs.jmedchem.0c01895
J. Med. Chem. 2021, 64, 4430−4449

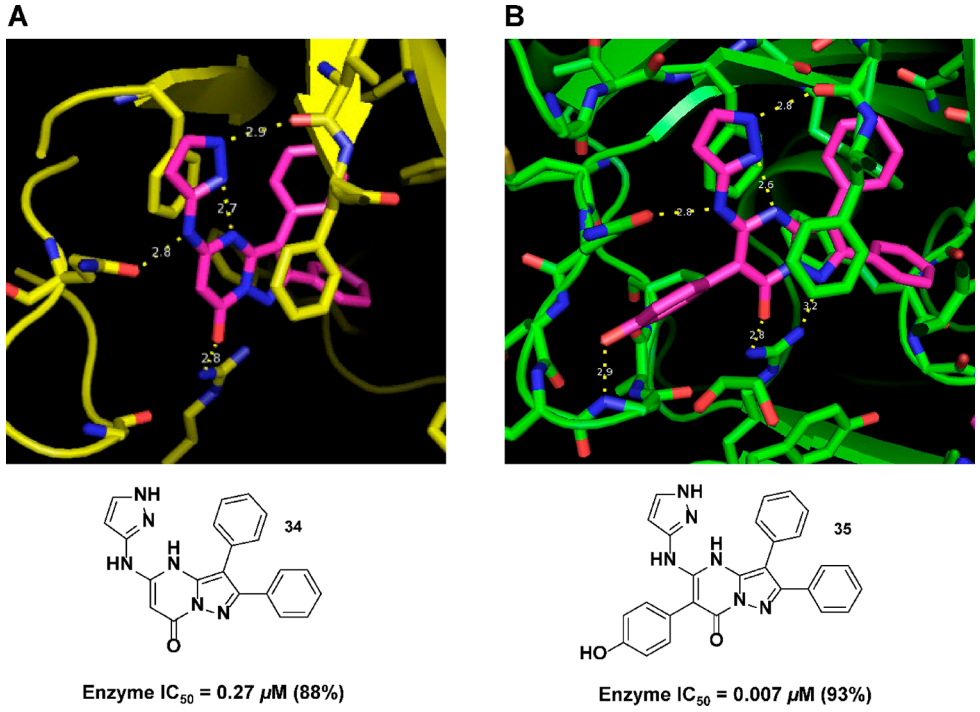

Figure 6. Intramolecular hydrogen bonding improves maximum percentage inhibition. (A) Cocrystal structure of MAT2A·SAM·**34** (PDB code 7KDA) identifies intramolecular hydrogen bond and new interaction with the MAT2A protein. (B) Cocrystal structure of MAT2A·SAM·**35** (PDB code 7KDB) confirms both the intramolecular hydrogen bond and the same new interactions seen with **34**.

Consistent with *in vitro* data, treatment with **AG-270** led to dose-dependent reductions in tumor SAM levels and tumor growth of KP4 *MTAP*-null xenografts (Figure 8B and 8C, TGI = 67% at 200 mg/kg, $p < 0.01$) and was well tolerated, with mean body weight loss <5% (Figure 8D). This *in vivo* study demonstrated that efficacy is related to SAM reduction (Figure 8C) and a range of 60−80% SAM reduction is adequate for maximal efficacy.

A similar study (being reported concurrently elsewhere) with mice bearing subcutaneous HCT116 *MTAP*-null xenografts was also conducted, and treatment with **AG-270** (200 mg/kg q.d.) led to a similar significant reduction in tumor growth (TGI = 75%, $p < 0.01$).[16] No antiproliferative effects were observed in HCT116 *MTAP*-WT tumor-bearing mice dosed equivalently with **AG-270**,[16] in line with the earlier results obtained with the *in vivo* tool compound **AGI-25696**. Further *in vivo* studies in patient-derived mouse xenograft models, along with mechanism-of-action studies, leading to rational combination therapies with **AG-270** and other anticancer treatment modalities have been reported.[16] Mouse and cynomolgus monkey safety studies established that **AG-270** has the desired preclinical safety profile to proceed to clinical studies (unpublished data). A phase I clinical trial investigating **AG-270** in advanced solid tumors or lymphomas with MTAP loss is currently underway (Clinicaltrials.gov identifier: NCT03435250).

CHEMISTRY

The synthetic route to **AG-270**, which is of general use to prepare related analogues, is described in Scheme 1A. The commercially available methyl 2-(4-methoxyphenyl) acetate **45** incorporating R_3 (step A of Scheme 1) is reacted with dimethyl carbonate in the presence of a suitable strong base such as potassium *tert*-butoxide to provide intermediate **46**. Dimethyl malonate **46** is reacted at high temperatures in a suitable solvent such as xylene with the 1H-pyrazol-5-amine **56** to provide the 5-hydroxy substituted pyrazolopyrimidinone **47**, bringing in the R_1 and R_2 substituents. Bicyclic intermediate **47** is reacted with phosphoryl chloride to provide the dichloride **48**. The 7-chloro group of **48** is selectively reacted with sodium methoxide to give the 7-methoxy intermediate **49**, which is aminated at the 5-position of the pyrazolopyrimidinone ring in step E by reacting with **50** in the presence of a palladium catalyst to give **51**. Finally, the 7-methoxy group is dealkylated to a ketone in step F to give the final product **AG-270**.

The synthesis of the 4-(cyclohex-1-en-1-yl)-3-phenyl-1H-pyrazol-5-amine **56** is outlined in Scheme 1B. A mixture of 3-oxo-3-phenylpropanenitrile **52** and 4-(methoxybenzyl)-hydrazine were reacted in acetic acid/ethanol to give the protected amino pyrazole **53**, followed by addition of cyclohexanone **54** in acetic acid to give 4-(cyclohex-1-en-1-yl)-1-(4-methoxybenzyl)-3-phenyl-1H-pyrazol-5-amine **55**. Final deprotection of the 4-methoxybenzyl group was carried out by trifluoromethanesulfonic anhydride in trifluoroacetic acid stirred at 30 °C to give the amino pyrazole **56**.

Other analogues were synthesized following Scheme 2A. A solution of the commercially available methyl 2-(quinolin-6-yl)acetate **57** was deprotonated with LDA and reacted with acetyl chloride **58** to give intermediate **59**. The mixture of intermediate **59** and amine **60** in acetic acid was reacted at 90 °C to generate the final product **AGI-25696**. Scheme 2 B describes the general synthesis of amine **60**. A solution of 2-phenylacetonitrile **61** and methyl benzoate **62** in THF was treated with sodium hydride to give intermediate **63**. A mixture of 3-oxo-2,3-diphenylpropanenitrile and hydrazine hydrate in acetic acid/ethanol were reacted to produce the amino pyrazole **60**.

https://doi.org/10.1021/acs.jmedchem.0c01895
J. Med. Chem. 2021, 64, 4430−4449

Table 7. Further R_4 Exploration Improves Cell Potency[a]

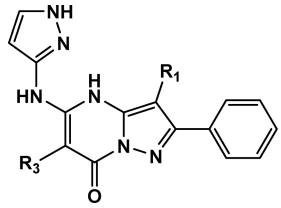

Compound	Structure of R_3	Structure of R_1	Enzymatic MAT2A IC_{50} (μM)	Enzymatic MAT2A maximal inhibition (%)	72 h cell *MTAP*-null SAM IC_{50} (μM)	Cell proliferation *MTAP*-null IC_{50} (μM)	ER, HLM	Human PPB (% bound)
35	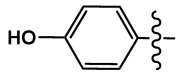	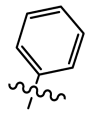	0.007	93	-	0.527	0.26	-
36	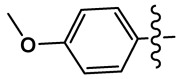	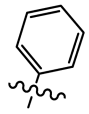	0.013	94	0.008	0.892	0.36	99.78
37	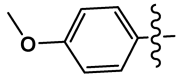		0.005	96	0.021	0.080	0.56	99.82
38	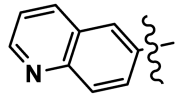		0.004	92	0.018	0.073	0.55	99.76
39	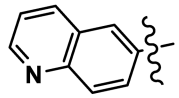	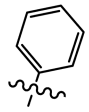	0.007	94	-	0.522	0.49	99.80

[a]Values for the biochemical and cell results are the mean of three experiments. ER = extraction ratio; HLM = human liver microsome.

Scheme 3 shows the general synthetic route for several additional compounds reported here. The intermediate **59**, methyl 3-oxo-2-(quinolin-6-yl)butanoate, prepared as in Scheme 2 (step A), was reacted with 3-phenyl-1H-pyrazol-5-amine **64** (step B) to generate intermediate **65**. 2-(Trimethylsilyl)ethoxymethyl (SEM) protection followed by NBS bromination gave intermediate **66**. Suzuki reaction of **66** with the R_1 intermediate **67** produced intermediate **68** and, after SEM deprotection, provided the final compound **69**.

CONCLUSIONS

Previous work investigating *MTAP* loss in cancer cells revealed that MTA accumulation sensitizes cells to short hairpin RNA-mediated depletion of MAT2A and the SAM-utilizing enzyme PRMT5. However, existing clinical-stage inhibitors of PRMT5 fail to recapitulate this *MTAP*-dependent effect, likely because the existing inhibitors have a SAM-uncompetitive mechanism that is not synergistic with MTA[21,22] and thus fail to selectively inhibit the proliferation of *MTAP*-null versus *MTAP*-WT cancer cells. In contrast, reduction of SAM levels via MAT2A inhibition can act synergistically with MTA elevation to selectively inhibit PRMT5 in *MTAP*-deleted cells, thereby inhibiting cell growth. Thus, the inhibition of MAT2A allows for the selective inhibition of PRMT5 activity in *MTAP*-null cancer cells and tumors by limiting the availability of SAM and is predicted to afford a greater therapeutic window than known PRMT5 inhibitors by limiting the potential toxicity of PRMT5 inhibition in normal, *MTAP*-WT tissues.[23−25]

We have described here the discovery of potent and selective inhibitors of MAT2A via structure-guided design, starting from a fragment with very low potency. Further, we have demonstrated that potent pharmacologic inhibition of MAT2A inhibits the growth of *MTAP*-deleted cancers *in vivo* with good tolerability, thus validating MAT2A as a therapeutic

https://doi.org/10.1021/acs.jmedchem.0c01895
J. Med. Chem. 2021, 64, 4430−4449

Table 8. Final R_4 Exploration Generates Compounds Having Balanced Properties

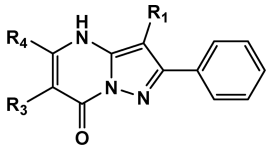

Compound	Structure of R_4	Structure of R_3	Structure of R_1	Enzymatic MAT2A IC_{50} (μM)	Enzymatic MAT2A maximal inhibition (%)	72 h cell *MTAP*-null SAM IC_{50} (μM)	Cell proliferation *MTAP*-null IC_{50} (μM)	ER, HLM	Human PPB (% bound)
40	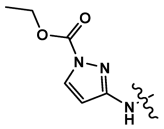	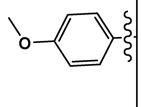		0.011	93	0.015	0.430	0.51	-
41	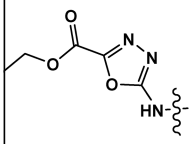	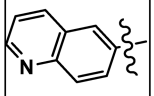		0.004	88	-	>20.0	0.70	-
42	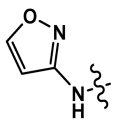	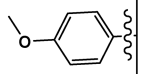		0.010	94	0.065	0.812	0.11	98.92
43	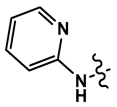	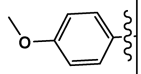		0.007	85	0.025	0.793	0.13	98.72
44	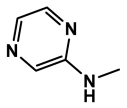	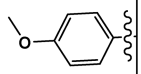		0.028	95	0.016	0.409	-	99.15
AG-270	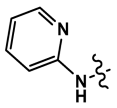	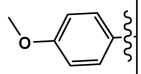		0.014	91	0.020	0.257	0.05	98.46

[a]Values for the biochemical and cell results are the mean of three experiments. ER = extraction ratio; HLM = human liver microsome.

target for a biomarker-selected patient population of significant size. On the basis of these discoveries, **AG-270**, an oral, first-in-class MAT2A inhibitor, has entered clinical development and is under investigation in a phase 1 trial that is currently enrolling patients with *MTAP*-deleted solid tumors and lymphomas (Clinical Trial NCT03435250).

EXPERIMENTAL SECTION

Chemistry. *General Experimental Notes.* In the following examples, all reagents were purchased from commercial sources (such as Alfa, Acros, Sigma-Aldrich, TCI, and Shanghai Chemical Reagent Company) and used without further purification. Flash chromatography was performed on an Ez Purifier III (Lisure Science Co., Ltd., China) using a column with silica gel particles of 200−300 mesh. Analytical and preparative TLC plates were HSGF 254 (0.15−0.2 mm thickness, Yucheng Chemical Co., Ltd. China). NMR spectra were obtained on a Bruker AMX-400 instrument. Chemical shifts were reported in parts per million (ppm, δ) downfield from tetramethylsilane. Mass spectra were obtained with ESI using a Waters LCT TOF mass spectrometer. HPLC was conducted using an Agilent 1200 liquid chromatography column (UltiMate 4.6 × 50 mm, 5 μm, mobile phase A: 0.1% formic acid in water; mobile phase B: acetonitrile). All compounds were assessed for purity by this reverse column HPLC method (photodiode-array detection at wavelengths of 254 and 280 nm) and shown to have purity >95%. Microwave reactions were run on a Biotage Initiator 2.5 microwave synthesizer.

The synthetic protocols and characterization of key intermediates in the synthesis of **AG-270** are included below. Synthesis of all other key analogues are reported in the Supporting Information.

https://doi.org/10.1021/acs.jmedchem.0c01895
J. Med. Chem. 2021, 64, 4430−4449

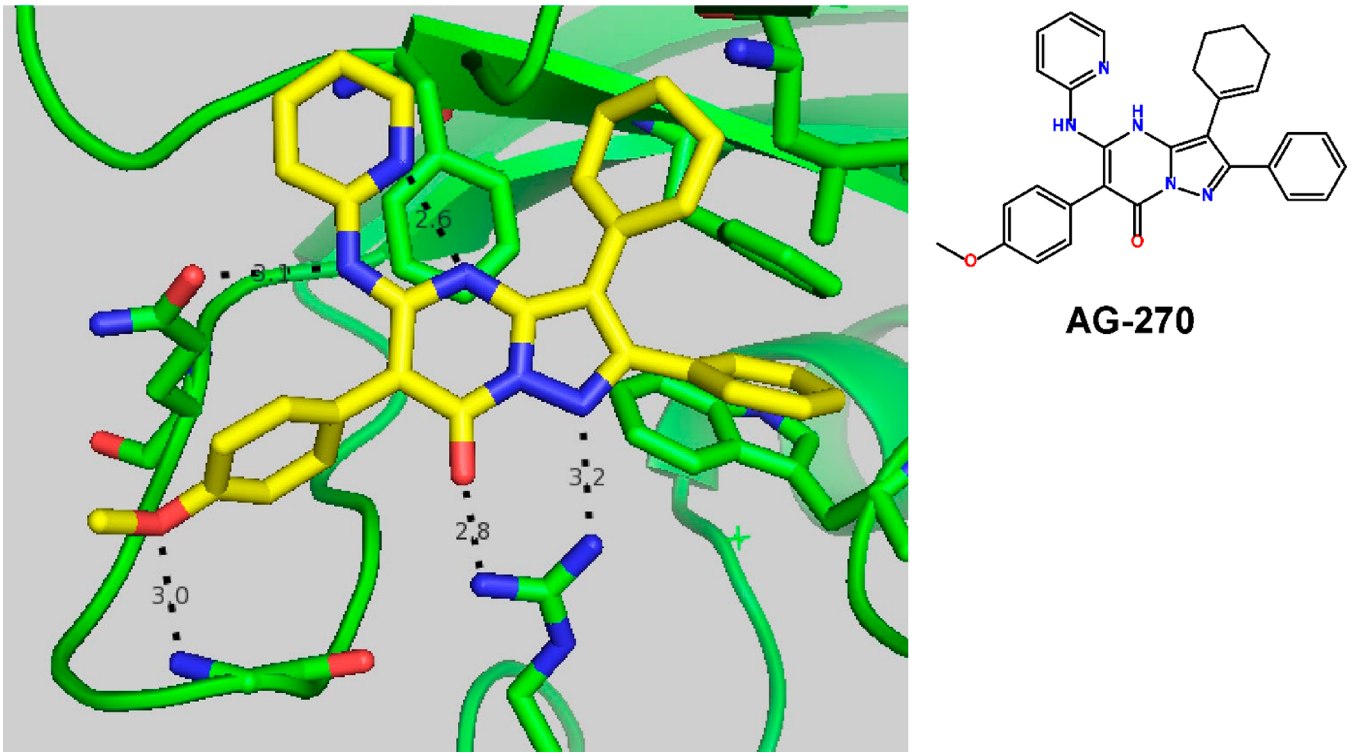

Figure 7. Cocrystal structure of **AG-270** (PDB code 7KCC). The crystal structure of **AG-270** (in yellow) confirms the binding mode, the intramolecular hydrogen bond, and all the key interactions with MAT2A.

Table 9. AG-270 Characterization: Enzymatic Activity, Cell Potency, and Cross-Species ADME Properties Show a Balance of Potency and Properties[a]

MAT2A enzyme IC_{50} (μM)	0.014
HCT116 *MTAP*-null cell SAM inhibition at 72 h IC_{50} (μM)	0.02
ER liver microsome, human/monkey/dog/rat/mouse	0.05/0.20/0/0.21/0.38
ER hepatocyte, human/monkey/dog/rat	0.16/0.13/0.12/0.18
Eh *in vivo*, monkey/dog/rat/mouse (1 mg/kg IV)	0.023/0.022/0.142/0.015
PPB, human/monkey/dog/rat/mouse (% free)	1.5/1.1/2.8/1.6/0.28
solubility (μM) pH 2/7.4[b]	<0.5/<1.0
Caco-2 permeability, A > B/efflux ratio (10^{-6}cm/s)[b]	0.13/0.76
Oral bioavailability at 5 mg/kg, monkey/dog/rat (%*F*)	31/48/92
PXR (fold activation at 10 μM)	3.6 (22% of rifampin)
UGT1A1 inhibition IC_{50} (μM)	1.1
OATP1B1 inhibition IC_{50} (μM)	2.1
CYP inhibition, 3A4/2C9/2C19/2D6/3A4 (μM)	all >10
CYP inactivation	>3.26× shift for 2B6 (15.6 and >50 μM ± NADPH); >50 μM for other CYPs

[a]Eh = hepatic extraction ratio; ER = extraction ratio. [b]Solubility measurements were unreliable; Caco-2 data are unreliable due to low recovery.

Synthesis of Key Pyrazolo-pyrimidine Analogues. The original fragment compound **1** was identified via MS-based detection of small fragments that bound to MAT2A in an affinity capture assay using an ultracentrifugation assay.[11] Further validation studies utilized compound **1** material purchased from Vitas-M (catalog number STK851087). Compound **2** was purchased in the hit expansion phase from Vitas-M (catalog number STK591300). Compounds AGI-24512 and AGI-25696 were synthesized as recently reported.[26,27]

Synthesis of AG-270 (Scheme 1 A). *Dimethyl 2-(4-Methoxyphenyl)malonate (**46**).* Step A: To dimethyl carbonate (3.2 L) was slowly added potassium *tert*-butoxide (500 g) at 0 °C and the mixture was stirred for 1 h at rt. Then, methyl 2-(4-methoxyphenyl)acetate **45** (400 g) was added dropwise over 2 h and stirred at rt overnight. The reaction was quenched with water (1.5 L), followed by extraction with ethyl acetate (1 L × 3). The combined organic layers were washed with brine (1 L), dried over anhydrous Na_2SO_4, and concentrated *in vacuo*. The residue was purified by flash chromatography eluting with petroleum ether/ethyl acetate (20/1−5/1) to obtain the desired product as a white solid (400 g, 75%). m/z = 239.1 $[M + H]^+$, LC-MS: m/z $[M + H]^+$ 239; ^{1}H NMR (400 MHz, chloroform-d): δ 7.33 (d, J = 8.6 Hz, 2H), 6.90 (d, J = 8.9 Hz, 2H), 4.61 (s, 1H), 3.80 (s, 3H), 3.75 (s, 6H).

*3-(Cyclohex-1-en-1-yl)-5-hydroxy-6-(4-methoxyphenyl)-2-phenylpyrazolo[1,5-a]pyrimidin-7(4H)-one (**47**).* Step B: To a solution of dimethyl 2-(4-methoxyphenyl)malonate **46** (39.6 g, 166 mmol) in tri-*n*-butylamine (80 mL) at 198 °C was added 4-cyclohexenyl-3-phenyl-1H-pyrazol-5-amine **56** (47.3 g, 199 mmol) in portions, and the resultant mixture was stirred for 1 h at 198 °C. The mixture was cooled to rt, and solvent was decanted. THF (150 mL) and HCl (6N, 600 mL) were added with stirring vigorously for 0.5 h. The precipitates were collected by filtration, washed with methanol, and dried under reduced pressure to give 3-(cyclohex-1-en-1-yl)-5-hydroxy-6-(4-methoxyphenyl)-2-phenylpyrazolo[1,5-*a*]pyrimidin-7(4H)-one **47** (48 g, 70%) as a yellow solid. m/z = 414.17 $[M + H]^+$, LC-MS: m/z 414.2 $[M + H]^+$; ^{1}H NMR (400 MHz, DMSO-d_6): δ 7.74 (d, J = 6.98 Hz, 2H), 7.31−7.49 (m, 5H), 6.94 (d, J = 8.60 Hz, 2H), 5.80 (br s, 1H), 3.78 (s, 3H), 2.15 (br s, 2H), 2.02 (br s, 2H), 1.65 (br s, 4H).

*5,7-Dichloro-3-(cyclohex-1-en-1-yl)-6-(4-methoxyphenyl)-2-phenylpyrazolo[1,5-a]pyrimidine (**48**).* Step C: A solution of 3-(cyclohex-1-en-1-yl)-5-hydroxy-6-(4-methoxyphenyl)-2-phenylpyrazolo[1,5-*a*]pyrimidin-7(4H)-one **47** (47.0 g, 104 mmol) in phosphorus oxychloride (100 mL) was stirred at reflux for 16 h. The solvent was removed *in vacuo*. The residue was added slowly to

https://doi.org/10.1021/acs.jmedchem.0c01895
J. Med. Chem. 2021, 64, 4430−4449

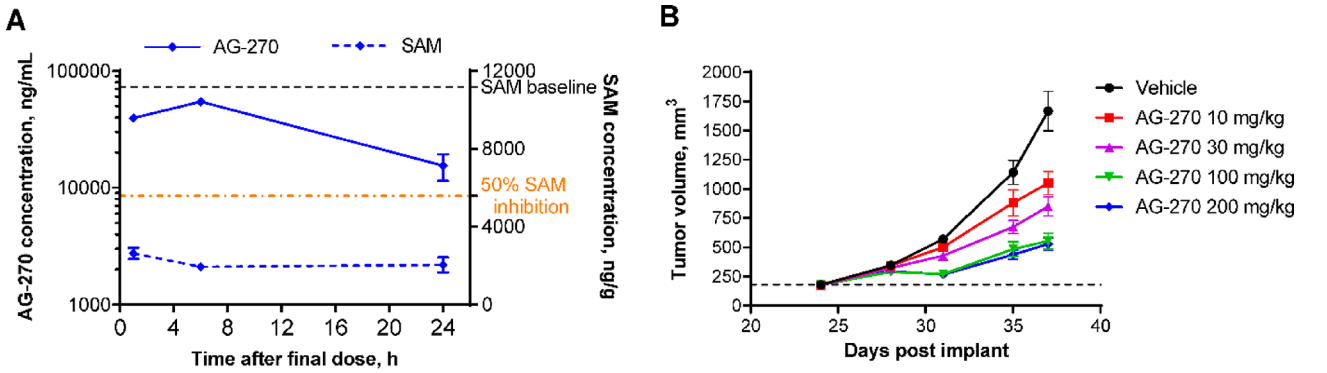

C

Group	TGI, %	[SAM] inhibition, %
10 mg/kg	36	33.4
30 mg/kg	48	44.7
100 mg/kg	66	63.5
200 mg/kg	67	81.1

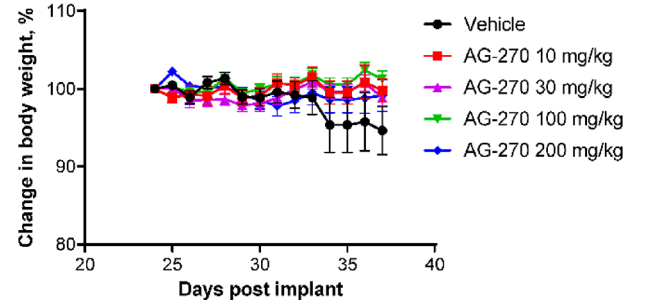

Figure 8. Dose-dependence study in KP4 xenograft mouse model reveals that maximal efficacy is related to SAM reduction. Twelve mice were used per arm (60 total animals) in this study. **AG-270** was given orally q.d. (on days 24−38) to mice inoculated subcutaneously with KP4 *MTAP*-null cells, and both compound and SAM levels were monitored. (A) Plasma pharmacokinetics of **AG-270** were monitored up to 24 h post last 200 mg/kg dose (solid blue line) and displayed very good coverage; tumor SAM levels were also monitored in the same time period and showed stable, low concentrations (blue dotted line). (B) Tumor volume over a 38-day study. (C) Tumor growth inhibition (TGI) and percentage tumor SAM reduction at various doses indicate that SAM reduction between 60 and 80% leads to the same level of TGI at ∼66%. Reduction in SAM concentration was dose dependent from 10 to 200 mg/kg and in tumor volume from 10 to 100 mg/kg. (D) Mean change in mouse body weight. Error bars show standard error of the mean.

Scheme 1. (A) Synthesis of AG-270 and (B) Synthesis of the 4-(Cyclohex-1-en-1-yl)-3-phenyl-1H-pyrazol-5-amine 56

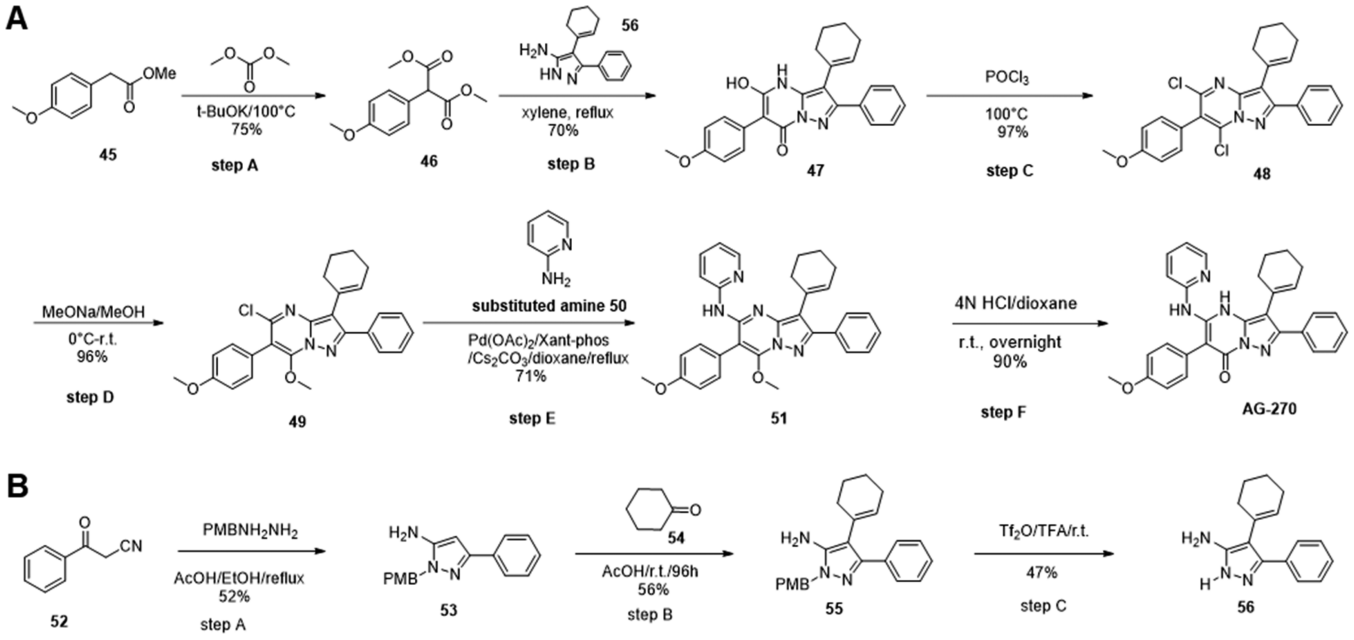

methanol (100 mL) cooled at 0 °C. The precipitates were collected by filtration, washed with methanol, and dried under reduced pressure to give 5,7-dichloro-3-(cyclohex-1-en-1-yl)-6-(4-methoxyphenyl)-2-phenylpyrazolo[1,5-*a*]pyrimidine (50 g, 97%) as a yellow solid. *m*/*z* 450.2 $[M + H]^+$, LC-MS: *m*/*z* 450.1 $[M + H]^+$; ^{1}H NMR (400 MHz, DMSO-d_6): δ 7.82 (d, J = 7.25 Hz, 2H), 7.36−7.56 (m, 5H), 7.10 (d, J = 8.60 Hz, 2H), 5.87 (br s, 1H), 3.84 (s, 3H), 2.20 (br s, 4H), 1.70 (d, J = 4.57 Hz, 4H).

*5-Chloro-3-(cyclohex-1-en-1-yl)-7-methoxy-6-(4-methoxyphenyl)-2-phenylpyrazolo[1,5-a]pyrimidine (**49**).* Step D: To a solution of 5,7-dichloro-3-(cyclohex-1-en-1-yl)-6-(4-methoxyphenyl)-2-

https://doi.org/10.1021/acs.jmedchem.0c01895
J. Med. Chem. 2021, 64, 4430−4449

Scheme 2. Synthesis of (A) AGI-25696 and (B) Amino Pyrazole 60

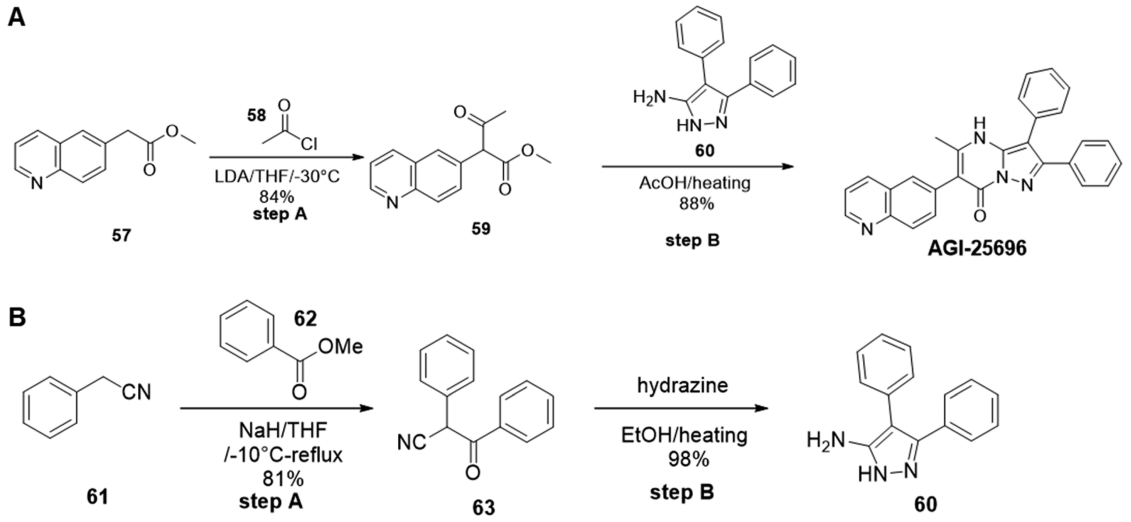

Scheme 3. General Synthetic Scheme for R_1 Analogues

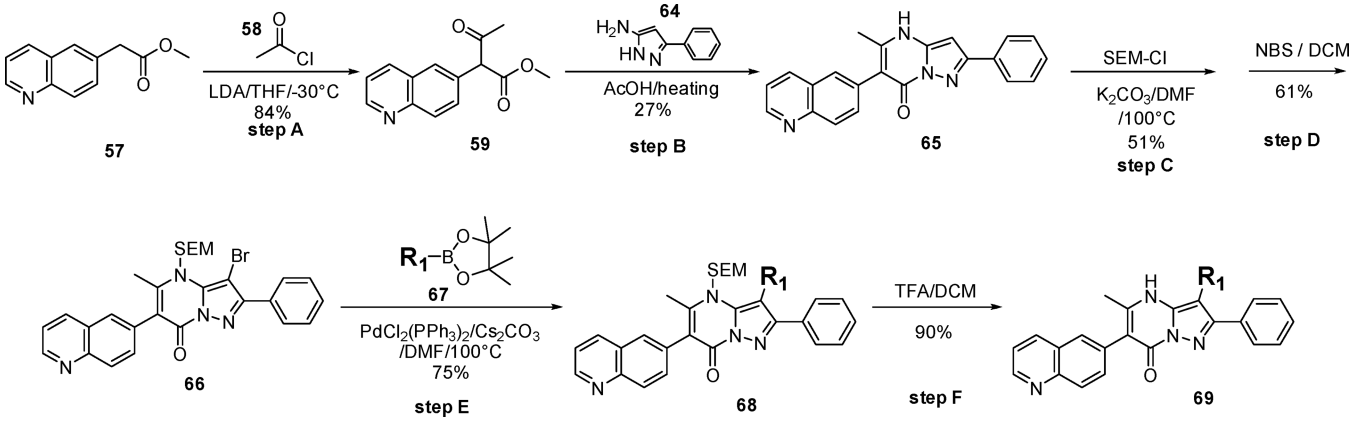

phenylpyrazolo[1,5-*a*]pyrimidine **48** (40 g, 88 mmol) in DCM (400 mL) at 0 °C was added sodium methoxide (30% in methanol, 80 g) dropwise. The resultant mixture was stirred for 10 min at 0 °C. The reaction was quenched by adding ice water (100 mL) and extracted with DCM (200 mL) three times. The combined organic layers were washed with brine (200 mL), dried over anhydrous Na_2SO_4, and concentrated *in vacuo*. The residue was suspended in methanol (50 mL). The precipitates were collected by filtration, washed with methanol, and dried under reduced pressure to give 5-chloro-3-(cyclohex-1-en-1-yl)-7-methoxy-6-(4-methoxyphenyl)-2-phenylpyrazolo[1,5-*a*]pyrimidine as a yellow solid (37.6 g, 96%). *m/z* 446.16 $[M + H]^+$, LC-MS: *m/z* 446.1 $[M + H]^+$; ^1H NMR (400 MHz, DMSO-d_6): δ 7.78−7.91 (m, 2H), 7.42−7.58 (m, 3H), 7.33−7.42 (m, *J* = 8.9 Hz, 2H), 7.00−7.14 (m, *J* = 8.9 Hz, 2H), 5.83 (br s, 1H), 4.14 (s, 3H), 3.84 (s, 3H), 2.20 (d, *J* = 5.9 Hz, 4H), 1.61−1.77 (m, 4H).

*3-(Cyclohex-1-en-1-yl)-6-(4-methoxyphenyl)-2-phenyl-5-(pyridin-2-ylamino)pyrazolo[1,5-a]pyrimidin-7(4H)-one (**51**).* Step E stoichiometry: 5-chloro-3-(cyclohex-1-en-1-yl)-7-methoxy-6-(4-methoxyphenyl)-2-phenylpyrazolo[1,5-*a*]pyrimidine (200 mg, 0.449 mol), pyridin-2-amine **50** (63.4 mg, 0.674 mol, 1.5 equiv), $Pd(OAc)_2$ (20.2 mg, 0.0898 mol, 0.2 equiv), Xantphos (52 mg, 0.0898 mol, 0.2 equiv) and K_2CO_3 (265 mg, 1.12 mol, 2.5 equiv) in dioxane (5 mL) under heating at 120 °C for 1 h under N_2 atmosphere. After workup, 160 mg (71%) was collected. *m/z* $[M + H]^+$ 504.2, LC-MS: *m/z* 504.3 $[M + H]^+$.

*3-(Cyclohex-1-en-1-yl)-6-(4-methoxyphenyl)-2-phenyl-5-(pyridin-2-ylamino)pyrazolo[1,5-a]pyrimidin-7(4H)-one (**AG-270**).* Step F: A solution of 3-(cyclohex-1-en-1-yl)-7-methoxy-6-(4-methoxyphenyl)-2-phenyl-N-(pyridin-2-yl)pyrazolo[1,5-*a*] pyrimidin-5-amine (**51**) (120 mg, 0.22 mol) in 4 M HCl/1.4-dioxane (3 mL) was stirred at rt for 16 h. The reaction mixture was basified with $NaHCO_3$ solution to pH = 8 and filtered to afford the title compound (97 mg, 90%). *m/z* $[M + H]^+$ 490.2, LC-MS: *m/z* 490.2 $[M + H]^+$; ^1H NMR (400 MHz, DMSO-d_6): δ 9.09 (br s, 1H), 8.20 (d, *J* = 4.3 Hz, 1H), 7.82 (t, *J* = 7.3 Hz, 1H), 7.73 (d, *J* = 7.3 Hz, 2H), 7.38−7.51 (m, 3H), 7.28−7.38 (m, 3H), 7.10−7.17 (m, 1H), 7.03 (d, *J* = 8.5 Hz, 2H), 6.06 (br s, 1H), 3.82 (s, 3H), 2.34 (br s, 2H), 2.06 (br s, 2H), 1.65−1.79 (m, 4H).

Molecular Modeling. All computations were carried out using the molecular operating environment (MOE).[14] All graphics are produced using PyMol.[28]

Biochemical Assays. *Cloning, Protein Expression, and Purification.* MAT2A protein for biochemical assay was expressed by recombinant baculovirus in SF9 cells using the Bac to Bac system cloned into the pFASTBAC1 vector (Invitrogen). Recombinant MAT2A was isolated from the cell lysate of 150 g of infected cells using high performance Ni Sepharose column chromatography. Recombinant MAT2A homodimer was eluted with 250 and 500 mM imidazole, and fractions containing MAT2A were identified by SDS-PAGE and pooled.

For crystallization, full-length MAT2A was cloned into a pET21a-based vector with N-terminal (His)6-tag and tobacco etch virus (TEV) protease cleavage site. The protein was expressed in *Escherichia coli* strain BL21 (DE3) with 0.5 mM isopropyl β-D-1-thiogalactopyranoside at 18 °C for 16 h. The cells were harvested, suspended in lysis buffer containing 20 mM Tris-HCl, pH 7.5, 500 mM NaCl, 5% glycerol, 1 mM tris(2-carboxyethyl) phosphine

https://doi.org/10.1021/acs.jmedchem.0c01895
J. Med. Chem. 2021, 64, 4430−4449

(TCEP), and opened by sonication. The supernatant was obtained by centrifugation and loaded on a nickel−nitrilotriacetic acid (Ni−NTA) column (Qiagen, Cat. #30230). The column was washed with buffer containing 20 and 50 mM imidazole in the lysis buffer prior to elution with 250 mM imidazole. (His)6-tag was cleaved by TEV protease (1:20 w/w ratio protease to protein) while dialyzing against the lysis buffer at 4 °C overnight. The sample was loaded onto an Ni−NTA column. The flow-through and eluate with 15 mM imidazole in the lysis buffer were collected and concentrated. The protein was further purified by HiLoad 16/600 Superdex 200 pg column (GE Healthcare Life Sciences) in the lysis buffer, concentrated to 24 mg/mL, and flash frozen with liquid nitrogen for storage.

Fragment Screening. Library screening was performed by ultrafiltration as previously described[11] using Centricon 10 mW cutoff devices (EMD Millipore). MAT2A protein at a concentration of 2 μM was incubated with mixtures of 20 compounds at 50 μM each in 20 mM Tris-HCl, pH 7.5, and 500 mM NaCl. Relative retention was determined after three successive rounds of concentration and redilution by LC-MS.

SPR Analysis. MAT2A protein was immobilized to CM5 sensor chips (GE Healthcare Life Sciences) via a covalently attached anti-His IgG (Qiagen). The chip surface was activated by 1-ethyl-3-(3-(dimethylamino)propyl)carbodiimide (EDC)/*N*-hydroxysuccinimide (NHS) in HBS-EP+ buffer at 10 μL/min for 540 s. Penta-anti-His IgG was diluted 1:10 in sodium acetate pH 5.0 and injected for 360 s. Active sites were then blocked with 1 mM ethanolamine-HCl. Final immobilization level was about ∼16 000 response units for each flow cell. MAT2A protein was captured on the prepared surface after dilution in running buffer (50 mM Tris pH 8.0, 150 mM NaCl, 10 mM $MgCl_2$, 0.005% P20, 0.5 mM TCEP), to a final capture level of about 7500 RU. Binding analysis was performed using a 100 mM stock compound solution prepared in DMSO diluted in running buffer.

IC50 Determinations. For determination of the inhibitory potency of compounds against the MAT2A homodimer, protein was diluted to 1.25 μg/mL in assay buffer (50 mM Tris, pH 8.0, 50 mM KCl, 15 mM $MgCl_2$, 0.3 mM EDTA, 0.005% [w/v] BSA). Test compound was prepared in 100% DMSO at 50× the desired final concentration. A 1 μL volume of compound dilution was added to 40 μL of enzyme dilution and the mixture was allowed to equilibrate for 60 min at 25 °C. The enzymatic assay was initiated by the addition of 10 μL of substrate mix (500 μM ATP, pH 7.0, 400 μM L-methionine in 1× assay buffer), and the mixture was incubated for a further 60 min at 25 °C. The reaction was halted and the liberated phosphate released by the enzyme in stoichiometric amounts by the production of SAM was measured using the PiColorLock Gold kit (Innova Biosciences). Absolute product amounts were determined by comparison with a standard curve of potassium phosphate buffer, pH 8.0.

Mechanism-of-Action Studies. To determine the mechanism-of-action[12] with regard to the L-methionine substrate, reactions were performed as described above with the modification that L-methionine substrate concentrations were varied in the final reaction from 6.25 to 400 μM, and the ATP concentration was set at 100 μM. For the determination of the mechanism-of-action with regard to ATP, reactions were performed as described above, with the modification that ATP was varied from 15 μM to 1 mM final concentration and L-methionine was fixed at 50 μM.

Crystallization, X-ray Data Collection, Processing, Structure Refinement, and Analysis. MAT2A·SAM complex was generated by mixing 20 mg/mL of MAT2A with 2 mM SAM and incubating on ice for 2 h. Crystals were obtained by hanging-drop vapor diffusion with 2 μL of MAT2A·SAM complex mixed with 1 μL of crystallization well buffer containing 0.2 M LiCl, 0.1 M Tris-HCl, pH 7.8−8.4, 16−22% PEG6000 and 10% ethylene glycol at 18 °C. Crystals of inhibitor complexes were obtained by cocrystallization by mixing 20 mg/mL of MAT2A with 2−25 mM of compound, followed by the addition of 2 mM SAM and incubation on ice for 2 h prior to crystallization as described above. The crystals were cryoprotected in the mother liquor with 10% DMSO and flash frozen in liquid nitrogen. The data for MAT2A·SAM·**2** crystal were collected at Advanced Photon Source beamline 21-ID-F with a Rayonix MX300 detector. MAT2A·SAM·**AGI-24512**, MAT2A·SAM·**34**, and MAT2A·SAM·**35** crystals were collected at the Shanghai Synchrotron Radiation Facility beamline BL17U1 with an ADSC Quantum 315r detector; MAT2A·SAM·**AG-270** crystal was collected at the Shanghai Synchrotron Radiation Facility beamline BL18U1 with a Pilatus3 6 M detector. All data were processed either with HKL2000[29] or XDS.[30] Initial phases were obtained by performing molecular replacement with the coordinates derived from PDB code 2P02 as a search template using Phaser[31] in CCP4 Suite. The restraints and coordinates of the compounds were generated by eLBOW.[32] Iterative model building was performed using COOT[33] and refined using REFMAC5[34] initially and using PHENIX[35] at the final stages. The data collection and structure refinement statistics are summarized in Supplemental Data Table 1. All inhibitors were modeled at an occupancy of 1.0 with the exception of inhibitor **2**, which was refined to an occupancy of 0.65. All structures contain one molecule of the ternary complex containing MAT2A, SAM and the inhibitor in the asymmetric unit. Dimeric MAT2A structures used in the analysis were generated by applying crystallographic symmetry operation. All figures representing structures were prepared with PyMOL.

■ ASSOCIATED CONTENT

Supporting Information

The Supporting Information is available free of charge at https://pubs.acs.org/doi/10.1021/acs.jmedchem.0c01895.

Cellular activity; mechanism-of-action studies; metabolic hotspot identification; enzymatic correlations; conformations; plasma concentration−time profiles; hydrophobicity and solubility correlations; crystallography data collection and refinement statistics; key pharmacokinetic parameters; cellular assay methods; *in vivo* study methods; synthetic procedures for select compounds; ^1H NMR spectra; HPLC and LC-MS chromatograms; AG-270 structures (PDF)

Molecular formula strings (CSV)

■ AUTHOR INFORMATION

Corresponding Author

Zenon Konteatis − *Agios Pharmaceuticals, Inc., Cambridge, Massachusetts 02139, United States;* orcid.org/0000-0002-5421-4907; Email: zenon.konteatis@agios.com

Authors

Jeremy Travins − *Agios Pharmaceuticals, Inc., Cambridge, Massachusetts 02139, United States*

Stefan Gross − *Agios Pharmaceuticals, Inc., Cambridge, Massachusetts 02139, United States*

Katya Marjon − *Agios Pharmaceuticals, Inc., Cambridge, Massachusetts 02139, United States*

Amelia Barnett − *Agios Pharmaceuticals, Inc., Cambridge, Massachusetts 02139, United States*

Everton Mandley − *Agios Pharmaceuticals, Inc., Cambridge, Massachusetts 02139, United States*

Brandon Nicolay − *Agios Pharmaceuticals, Inc., Cambridge, Massachusetts 02139, United States*

Raj Nagaraja − *Agios Pharmaceuticals, Inc., Cambridge, Massachusetts 02139, United States*

Yue Chen − *Agios Pharmaceuticals, Inc., Cambridge, Massachusetts 02139, United States*

Yabo Sun − *Viva Biotech, Shanghai 201203, China*

Zhixiao Liu − *Viva Biotech, Shanghai 201203, China*

Jie Yu − *Viva Biotech, Shanghai 201203, China*

Zhixiong Ye − *Viva Biotech, Shanghai 201203, China*

Fan Jiang − *Viva Biotech, Shanghai 201203, China*
Wentao Wei − *Viva Biotech, Shanghai 201203, China*
Cheng Fang − *ChemPartner, Shanghai 201203, China*
Yi Gao − *ChemPartner, Shanghai 201203, China*
Peter Kalev − *Agios Pharmaceuticals, Inc., Cambridge, Massachusetts 02139, United States*
Marc L. Hyer − *Agios Pharmaceuticals, Inc., Cambridge, Massachusetts 02139, United States*
Byron DeLaBarre − *Agios Pharmaceuticals, Inc., Cambridge, Massachusetts 02139, United States*
Lei Jin − *Agios Pharmaceuticals, Inc., Cambridge, Massachusetts 02139, United States*
Anil K. Padyana − *Agios Pharmaceuticals, Inc., Cambridge, Massachusetts 02139, United States*
Lenny Dang − *Agios Pharmaceuticals, Inc., Cambridge, Massachusetts 02139, United States*
Joshua Murtie − *Agios Pharmaceuticals, Inc., Cambridge, Massachusetts 02139, United States*
Scott A. Biller − *Agios Pharmaceuticals, Inc., Cambridge, Massachusetts 02139, United States*
Zhihua Sui − *Agios Pharmaceuticals, Inc., Cambridge, Massachusetts 02139, United States*
Kevin M. Marks − *Agios Pharmaceuticals, Inc., Cambridge, Massachusetts 02139, United States*

Complete contact information is available at: https://pubs.acs.org/10.1021/acs.jmedchem.0c01895

Author Contributions

[#]Z.K. and J.T. contributed equally to this work.

Notes

The authors will release the crystallographic atomic coordinates and experimental data upon article publication (PDB codes 7KCE, 7KDA, 7KCF, 7KDB, and 7KCC).

The authors declare the following competing financial interest(s): All Agios authors were employees and stockholders at the time of the study.

■ ACKNOWLEDGMENTS

Agios Pharmaceuticals, Inc. funded these studies. Editorial assistance was provided by Christine Ingleby, PhD, CMPP, of Excel Medical Affairs, Horsham, UK, and supported by Agios Pharmaceuticals, Inc.

■ ABBREVIATIONS USED

Eh, hepatic extraction ratio; ER, extraction ratio; HLM, human liver microsome; K_D, dissociation constant calculated for SPR data; MAT2A, methionine adenosyltransferase 2A; MLM, mouse liver microsome; MTA, 5′-methylthioadenosine; MTAP, methylthioadenosine phosphorylase; Ni−NTA, nickel−nitrilotriacetic acid; PRMT5, protein arginine *N*-methyltransferase 5; SAM, *S*-adenosyl methionine; SEM, 2-(trimethylsilyl)ethoxymethyl; SPR, surface plasmon resonance; TEV, tobacco etch virus; TGI, tumor growth inhibition

■ REFERENCES

(1) Crespo, I.; Tao, H.; Nieto, A. B.; Rebelo, O.; Domingues, P.; Vital, A. L.; Patino Mdel, C.; Barbosa, M.; Lopes, M. C.; Oliveira, C. R.; Orfao, A.; Tabernero, M. D. Amplified and homozygously deleted genes in glioblastoma: impact on gene expression levels. *PLoS One* **2012**, *7*, No. e46088.

(2) Marjon, K.; Cameron, M. J.; Quang, P.; Clasquin, M. F.; Mandley, E.; Kunii, K.; McVay, M.; Choe, S.; Kernytsky, A.; Gross, S.; Konteatis, Z.; Murtie, J.; Blake, M. L.; Travins, J.; Dorsch, M.; Biller, S. A.; Marks, K. M. *MTAP* deletions in cancer create vulnerability to targeting of the MAT2A/PRMT5/RIOK1 axis. *Cell Rep.* **2016**, *15*, 574−587.

(3) Powell, E. L.; Leoni, L. M.; Canto, M. I.; Forastiere, A. A.; Iocobuzio-Donahue, C. A.; Wang, J. S.; Maitra, A.; Montgomery, E. Concordant loss of MTAP and p16/CDKN2A expression in gastroesophageal carcinogenesis: evidence of homozygous deletion in esophageal noninvasive precursor lesions and therapeutic implications. *Am. J. Surg. Pathol.* **2005**, *29*, 1497−1504.

(4) Zhang, H.; Chen, Z. H.; Savarese, T. M. Codeletion of the genes for *p16INK4*, methylthioadenosine phosphorylase, interferon-α1, interferon-β1, and other 9p21 markers in human malignant cell lines. *Cancer Genet. Cytogenet.* **1996**, *86*, 22−28.

(5) Kryukov, G. V.; Wilson, F. H.; Ruth, J. R.; Paulk, J.; Tsherniak, A.; Marlow, S. E.; Vazquez, F.; Weir, B. A.; Fitzgerald, M. E.; Tanaka, M.; Bielski, C. M.; Scott, J. M.; Dennis, C.; Cowley, G. S.; Boehm, J. S.; Root, D. E.; Golub, T. R.; Clish, C. B.; Bradner, J. E.; Hahn, W. C.; Garraway, L. A. *MTAP* deletion confers enhanced dependency on the PRMT5 arginine methyltransferase in cancer cells. *Science* **2016**, *351*, 1214−1218.

(6) Mavrakis, K. J.; McDonald, E. R., 3rd; Schlabach, M. R.; Billy, E.; Hoffman, G. R.; deWeck, A.; Ruddy, D. A.; Venkatesan, K.; Yu, J.; McAllister, G.; Stump, M.; deBeaumont, R.; Ho, S.; Yue, Y.; Liu, Y.; Yan-Neale, Y.; Yang, G.; Lin, F.; Yin, H.; Gao, H.; Kipp, D. R.; Zhao, S.; McNamara, J. T.; Sprague, E. R.; Zheng, B.; Lin, Y.; Cho, Y. S.; Gu, J.; Crawford, K.; Ciccone, D.; Vitari, A. C.; Lai, A.; Capka, V.; Hurov, K.; Porter, J. A.; Tallarico, J.; Mickanin, C.; Lees, E.; Pagliarini, R.; Keen, N.; Schmelzle, T.; Hofmann, F.; Stegmeier, F.; Sellers, W. R. Disordered methionine metabolism in MTAP/CDKN2A-deleted cancers leads to dependence on PRMT5. *Science* **2016**, *351*, 1208−1213.

(7) Lombardini, J. B.; Coulter, A. W.; Talalay, P. Analogues of methionine as substrates and inhibitors of the methionine adenosyltransferase reaction. Deductions concerning the conformation of methionine. *Mol. Pharmacol.* **1970**, *6*, 481−499.

(8) Lombardini, J. B.; Sufrin, J. R. Chemotherapeutic potential of methionine analogue inhibitors of tumor-derived methionine adenosyltransferases. *Biochem. Pharmacol.* **1983**, *32*, 489−495.

(9) Sviripa, V. M.; Zhang, W.; Balia, A. G.; Tsodikov, O. V.; Nickell, J. R.; Gizard, F.; Yu, T.; Lee, E. Y.; Dwoskin, L. P.; Liu, C.; Watt, D. S. 2′,6′-Dihalostyrylanilines, pyridines, and pyrimidines for the inhibition of the catalytic subunit of methionine S-adenosyltransferase-2. *J. Med. Chem.* **2014**, *57*, 6083−6091.

(10) Quinlan, C. L.; Kaiser, S. E.; Bolanos, B.; Nowlin, D.; Grantner, R.; Karlicek-Bryant, S.; Feng, J. L.; Jenkinson, S.; Freeman-Cook, K.; Dann, S. G.; Wang, X.; Wells, P. A.; Fantin, V. R.; Stewart, A. E.; Grant, S. K. Targeting S-adenosylmethionine biosynthesis with a novel allosteric inhibitor of Mat2A. *Nat. Chem. Biol.* **2017**, *13*, 785−792.

(11) Shibata, S.; Zhang, Z.; Korotkov, K. V.; Delarosa, J.; Napuli, A.; Kelley, A. M.; Mueller, N.; Ross, J.; Zucker, F. H.; Buckner, F. S.; Merritt, E. A.; Verlinde, C. L. M. J.; Van Voorhis, W. C.; Hol, W. G. J.; Fan, E. Screening a fragment cocktail library using ultrafiltration. *Anal. Bioanal. Chem.* **2011**, *401*, 1585.

(12) Copeland, R. A. *Evaluation of Enzyme Inhibitors in Drug Discovery: A Guide for Medicinal Chemists and Pharmacologists.*, 2nd ed.; Wiley: New York, 2013; pp 345−382.

(13) Shafqat, N.; Muniz, J. R. C.; Pilka, E. S.; Papagrigoriou, E.; von Delft, F.; Oppermann, U.; Yue, W. W. Insight into S-adenosylmethionine biosynthesis from the crystal structures of the human methionine adenosyltransferase catalytic and regulatory subunits. *Biochem. J.* **2013**, *452*, 27−36.

(14) *Molecular Operating Environment (MOE)*; Chemical Computing Group Inc.: Montreal, QC, Canada, 2016.

(15) Murray, B.; Antonyuk, S. V.; Marina, A.; Lu, S. C.; Mato, J. M.; Hasnain, S. S.; Rojas, A. L. Crystallography captures catalytic steps in human methionine adenosyltransferase enzymes. *Proc. Natl. Acad. Sci. U. S. A.* **2016**, *113*, 2104−9.

(16) Kalev, P.; Hyer, L. M.; Gross, S.; Konteatis, Z.; Chen, C.-C.; Fletcher, M.; Lein, M.; Aguado-Fraile, E.; Frank, V.; Barnett, A.; Mandley, E.; Goldford, J.; Chen, Y.; Sellers, K.; Hayes, S.; Lizotte, K.; Quang, P.; Tuncay, Y.; Clasquin, M.; Peters, R.; Weier, J.; Simone, E.; Murtie, J.; Liu, W.; Nagaraja, R.; Dang, L.; Sui, Z.; Biller, S. A.; Travins, J.; Marks, K. M.; Marjon, K. MAT2A inhibition blocks the growth of MTAP-deleted cancer cells by reducing PRMT5-dependent mRNA splicing and inducing DNA damage. *Cancer Cell* **2021**, *39*, 209−224.
(17) Kuhn, B.; Mohr, P.; Stahl, M. Intramolecular hydrogen bonding in medicinal chemistry. *J. Med. Chem.* **2010**, *53*, 2601−2611.
(18) Nielsen, D. S.; Shepherd, N. E.; Xu, W.; Lucke, A. J.; Stoermer, M. J.; Fairlie, D. P. Orally absorbed cyclic peptides. *Chem. Rev.* **2017**, *117*, 8094−8128.
(19) Giordanetto, F.; Tyrchan, C.; Ulander, J. Intramolecular hydrogen bond expectations in medicinal chemistry. *ACS Med. Chem. Lett.* **2017**, *8*, 139−142.
(20) Leuner, C.; Dressman, J. Improving drug solubility for oral delivery using solid dispersions. *Eur. J. Pharm. Biopharm.* **2000**, *50*, 47−60.
(21) Chan-Penebre, E.; Kuplast, K. G.; Majer, C. R.; Boriack-Sjodin, P. A.; Wigle, T. J.; Johnston, L. D.; Rioux, N.; Munchhof, M. J.; Jin, L.; Jacques, S. L.; West, K. A.; Lingaraj, T.; Stickland, K.; Ribich, S. A.; Raimondi, A.; Scott, M. P.; Waters, N. J.; Pollock, R. M.; Smith, J. J.; Barbash, O.; Pappalardi, M.; Ho, T. F.; Nurse, K.; Oza, K. P.; Gallagher, K. T.; Kruger, R.; Moyer, M. P.; Copeland, R. A.; Chesworth, R.; Duncan, K. W. A selective inhibitor of PRMT5 with *in vivo* and *in vitro* potency in MCL models. *Nat. Chem. Biol.* **2015**, *11*, 432−437.
(22) Fedoriw, A.; Rajapurkar, S. R.; O'Brien, S.; Gerhart, S. V.; Mitchell, L. H.; Adams, N. D.; Rioux, N.; Lingaraj, T.; Ribich, S. A.; Pappalardi, M. B.; Shah, N.; Laraio, J.; Liu, Y.; Butticello, M.; Carpenter, C. L.; Creasy, C.; Korenchuk, S.; McCabe, M. T.; McHugh, C. F.; Nagarajan, R.; Wagner, C.; Zappacosta, F.; Annan, R.; Concha, N. O.; Thomas, R. A.; Hart, T. K.; Smith, J. J.; Copeland, R. A.; Moyer, M. P.; Campbell, J.; Stickland, K.; Mills, J.; Jacques-O'Hagan, S.; Allain, C.; Johnston, D.; Raimondi, A.; Porter Scott, M.; Waters, N.; Swinger, K.; Boriack-Sjodin, A.; Riera, T.; Shapiro, G.; Chesworth, R.; Prinjha, R. K.; Kruger, R. G.; Barbash, O.; Mohammad, H. P. Anti-tumor activity of the type I PRMT inhibitor, GSK3368715, synergizes with PRMT5 inhibition through MTAP loss. *Cancer Cell* **2019**, *36*, 100−114.
(23) Bezzi, M.; Teo, S. X.; Muller, J.; Mok, W. C.; Sahu, S. K.; Vardy, L. A.; Bonday, Z. Q.; Guccione, E. Regulation of constitutive and alternative splicing by PRMT5 reveals a role for *Mdm4* pre-mRNA in sensing defects in the spliceosomal machinery. *Genes Dev.* **2013**, *27*, 1903−1916.
(24) Liu, F.; Cheng, G.; Hamard, P.-J.; Greenblatt, S.; Wang, L.; Man, N.; Perna, F.; Xu, H.; Tadi, M.; Luciani, L.; Nimer, S. D. Arginine methyltransferase PRMT5 is essential for sustaining normal adult hematopoiesis. *J. Clin. Invest.* **2015**, *125*, 3532−3544.
(25) Tee, W.-W.; Pardo, M.; Theunissen, T. W.; Yu, L.; Choudhary, J. S.; Hajkova, P.; Surani, M. A. Prmt5 is essential for early mouse development and acts in the cytoplasm to maintain ES cell pluripotency. *Genes Dev.* **2010**, *24*, 2772−2777.
(26) Konteatis, Z. D.; S, Z.; Travins, J. M.; Ye, Z. Pyrazolo[1,5-a]pyrimidin-7(4H)-ones as Inhibitors of Cellular Metabolic Processes and Their Preparation. Patent US 20180079753 A1 US 20180322, 2018.
(27) Konteatis, Z. D.; S, Z.; Travins, J. M.; Ye, Z. Preparation of Pyrazolo[1,5-a]pyrimidin-7(4H)-ones as Methionine Adenosyltransferase 2A Inhibitors for Treatment of Cancer. Patent WO 2018045071 A1 WO 20180308, 2018.
(28) *The PyMOL Molecular Graphics System, Version 2.0*; Schrödinger LLC: New York, NY.
(29) Otwinowski, Z.; Minor, W. Processing of X-ray diffraction data collected in oscillation mode. *Methods Enzymol.* **1997**, *276*, 307−326.
(30) Kabsch, W. XDS. *Acta Crystallogr., Sect. D: Biol. Crystallogr.* **2010**, *66*, 125−132.
(31) McCoy, A. J.; Grosse-Kunstleve, R. W.; Adams, P. D.; Winn, M. D.; Storoni, L. C.; Read, R. J. Phaser crystallographic software. *J. Appl. Crystallogr.* **2007**, *40*, 658−674.
(32) Moriarty, N. W.; Grosse-Kunstleve, R. W.; Adams, P. D. electronic Ligand Builder and Optimization Workbench (eLBOW): a tool for ligand coordinate and restraint generation. *Acta Crystallogr., Sect. D: Biol. Crystallogr.* **2009**, *65*, 1074−1080.
(33) Emsley, P.; Lohkamp, B.; Scott, W. G.; Cowtan, K. Features and development of Coot. *Acta Crystallogr., Sect. D: Biol. Crystallogr.* **2010**, *66*, 486−501.
(34) Murshudov, G. N.; Skubák, P.; Lebedev, A. A.; Pannu, N. S.; Steiner, R. A.; Nicholls, R. A.; Winn, M. D.; Long, F.; Vagin, A. A. *REFMAC5* for the refinement of macromolecular crystal structures. *Acta Crystallogr., Sect. D: Biol. Crystallogr.* **2011**, *67*, 355−367.
(35) Adams, P. D.; Afonine, P. V.; Bunkóczi, G.; Chen, V. B.; Davis, I. W.; Echols, N.; Headd, J. J.; Hung, L. W.; Kapral, G. J.; Grosse-Kunstleve, R. W.; McCoy, A. J.; Moriarty, N. W.; Oeffner, R.; Read, R. J.; Richardson, D. C.; Richardson, J. S.; Terwilliger, T. C.; Zwart, P. H. PHENIX: a comprehensive Python-based system for macromolecular structure solution. *Acta Crystallogr., Sect. D: Biol. Crystallogr.* **2010**, *66*, 213−221.

https://doi.org/10.1021/acs.jmedchem.0c01895
J. Med. Chem. 2021, 64, 4430−4449